Kinetochore- and chromosome-driven transition of microtubules into bundles promotes spindle assembly

Jurica Matković[1], Subhadip Ghosh[2], Mateja Ćosić[1], Marin Barišić[3,4], Nenad Pavin[2], Iva M. Tolić[1*]

[1]Division of Molecular Biology, Ruđer Bošković Institute, 10000 Zagreb, Croatia
[2]Department of Physics, Faculty of Science, University of Zagreb, 10000 Zagreb, Croatia
[3]Cell Division and Cytoskeleton, Danish Cancer Society Research Center, 2100 Copenhagen, Denmark
[4]Department of Cellular and Molecular Medicine, Faculty of Health Sciences, University of Copenhagen, 2200 Copenhagen, Denmark

*Correspondence to: tolic@irb.hr

ABSTRACT

Mitotic spindle assembly is crucial for chromosome segregation and relies on bundles of microtubules that extend from the poles and overlap in the middle. However, how these structures form remains poorly understood. Here we show that overlap bundles arise through a network-to-bundles transition driven by kinetochores and chromosomes. STED super-resolution microscopy revealed that PRC1-crosslinked microtubules initially form loose arrays, which become rearranged into bundles. Kinetochores promote microtubule bundling by lateral binding via CENP-E/kinesin-7 in an Aurora B-regulated manner. Bundle separation is driven by steric interactions of the bundle-associated chromosomes at the spindle midplane since spindles with uncondensed or uncongressed chromosomes are narrower. In agreement with experiments, theoretical modeling suggests that bundles arise through competing attractive and repulsive mechanisms. Finally, perturbation of overlap bundles led to inefficient correction of erroneous kinetochore-microtubule attachments. Thus, kinetochores and chromosomes drive coarsening of a uniform microtubule array into overlap bundles, which promote not only spindle formation but also chromosome segregation fidelity.

INTRODUCTION

Segregation of chromosomes during mitosis relies on the mitotic spindle, a supramolecular micro-machine made of microtubules and numerous microtubule-associated proteins, which is built de novo in each cell cycle[1]. While some spindle microtubules exist as individual filaments, such as astral microtubules, many are organized in bundles, such as kinetochore fibers and overlap bundles[2,3]. Kinetochore fibers are bundles of parallel microtubules that attach in an end-on manner to the kinetochore on the centromere of each chromosome, and link the kinetochore with the spindle pole[4,5]. Overlap or interpolar bundles consist of antiparallel microtubules that extend from the opposite spindle halves[6]. Spindle assembly has been extensively studied with focus on kinetochore dynamics and the formation of kinetochore fibers[7–12], whereas the mechanism of overlap bundle formation remains poorly understood.

Overlap bundles are essential for spindle assembly, as inhibition of the Eg5/kinesin-5 motor protein, which slides apart the antiparallel microtubules within the bundle, leads to monopolar spindles[13–16]. Such spindles without overlap bundles cannot segregate the chromosomes even though they usually contain kinetochore fibers, highlighting the indispensable role of overlap bundles in spindle functioning. In a mature spindle in metaphase, overlap bundles link sister kinetochore fibers like a bridge and because of this interaction are known as bridging fibers[17]. Their functions include balancing the tension on kinetochores[17–21], promoting chromosome alignment at the spindle midplane[22,23] and driving spindle elongation and chromosome segregation in anaphase[24–28]. Microtubules within bridging fibers are linked by the protein regulator of cytokinesis 1 (PRC1)[17,21,29], a crosslinker that has a 10-fold preference for antiparallel versus parallel microtubule overlaps *in vitro*[30–33]. Such crosslinkers together with motor proteins may drive the formation of initial overlaps between two antiparallel microtubules, as shown by computer simulations[34–37].

Mitotic spindles of human cells are made of more than 6000 microtubules[38]. In general, microtubules present in large numbers can exist in different phases, from loose networks to tight bundles, where the networks can be isotropic if the filaments are unoriented, nematic if the filaments are parallel and point either way, or polar if they point in a common direction[39]. Different types of microtubule networks have been studied in vitro[40–42], together with theoretical studies that explored under what conditions certain types of polymer networks appear or undergo a transition to bundles[43–47]. Yet, whether similar transitions occur in cells and what biological function they may have are open questions.

In this work we develop an assay for bundle formation, together with a theoretical model, and show that microtubules crosslinked by PRC1 undergo a network-to-bundles transition during early stages of spindle assembly. We find that this transition is stimulated by kinetochores, which promote microtubule bundling by binding to them laterally via CENP-E in a manner regulated by Aurora B. We further show that the separation of the bundles, which leads to spindle widening and the characteristic spindle shape, is driven by steric interactions of the chromosomes bound to the bundles as they congress to the spindle midplane, based on our findings that spindles with uncondensed or incompletely congressed chromosomes are narrower. Moreover, we identify a function of overlap bundles in the correction of erroneous kinetochore-microtubule attachments. Our work thus reveals that kinetochores and chromosomes together with crosslinkers drive coarsening of an initially uniform microtubule array into neatly organized overlap bundles, which not only support spindle assembly but also promote error-free mitosis.

RESULTS

The network of PRC1-crosslinked microtubules undergoes a transition to bundles

The overarching question of how the cell generates microtubule bundles that form the spindle shape contains two parts: how individual bundles are formed and what determines their separation. To study individual bundle formation, we first explored microtubule organization during early stages of mitosis by using stimulated emission depletion (STED) microscopy[48] to obtain super-resolution images of microtubules, together with the microtubule crosslinker PRC1 and chromosomes (Fig. 1a). The spatial pattern of microtubules and PRC1 changed profoundly during spindle formation and maturation (Fig. 1a). In early prometaphase characterized by the "prometaphase rosette" where the chromosomes are arranged like flower petals along the edge of the nascent spindle[49,50], the majority of spindle body microtubules appeared as a diffuse array with a few bundles present mainly at the edges ("Rosette" in Fig. 1a and Extended Data Fig. 1a). During late prometaphase, when chromosomes increasingly congress to the equatorial plane, and afterwards in metaphase, additional microtubule bundles appeared and their spacing became more regular, which was accompanied by the appearance of PRC1 stripes along the bundles ("Congression" and "Metaphase" in Fig. 1a and Extended Data Fig. 1a).

By looking at cross-sections of vertically oriented spindles, we found that microtubules of the spindle body are initially uniformly distributed over a ring-shaped region, and astral microtubules extend radially outwards (Fig. 1a end-on view). The spindle body microtubules became rearranged into discrete bundles that fill the spindle cross-section at an even spacing (end-on view in Fig. 1a and Extended Data Fig. 1a). Similarly, PRC1 distribution changed from a nearly homogeneous scattering over the ring-shaped region, which we call PRC1 network, to spot-like structures that colocalized with the microtubule bundles (end-on view in Fig. 1a and Extended Data Fig. 1a).

To study how a loose microtubule array transforms into bundles, we developed a live-cell assay termed "bundling assay" based on PRC1 as a marker of microtubule overlaps, where we imaged cross-sections of vertically oriented spindles in HeLa cells expressing PRC1-GFP starting at the rosette stage for 10 minutes (Fig. 1b). The rosette was identified by a chromosome circle surrounding the spindle, which was not yet fully closed (Extended Data Fig. 1b top and Fig. 1a bottom left). Time-lapse images revealed that the spatial distribution of PRC1 in the spindle cross-section gradually changes from a homogeneous dispersion over a ring-shaped area (PRC1 network) to discrete clusters (Fig. 1b and Supplementary Video 1), in agreement with STED images of fixed cells. Segmentation analysis (Methods; Extended Data Fig. 1c,d) showed that the number of PRC1-labeled segments and their mean PRC1-GFP intensity increased over time, whereas the segment area decreased (Fig. 1c,d and Extended Data Fig. 1e).

Intensity profiles of PRC1 along the ring-shaped area indicate that in comparison with the nearly constant PRC1 intensity in the rosette, the intensity at a later stage exhibited higher peaks and deeper valleys (t=0 vs. 7.2 minutes, Fig. 1e,f). The mean intensity did not change substantially, but the standard deviation increased 2.6-fold (n=10, Fig. 1g and Extended Data Fig. 1f). This suggests that the nearly uniform PRC1-labeled microtubule network undergoes a transition to bundles that accumulate PRC1, leaving the space between the bundles almost free from PRC1.

We next asked how the initial PRC1 network is formed. A large fraction of spindle microtubules is nucleated by the augmin complex at the wall of other microtubules[51,52]. When we used the bundling assay on cells depleted of the augmin subunit Haus6, we found that, in contrast to untreated cells, a PRC1 network was absent at the rosette stage (Extended Data Fig. 1g-i and Supplementary Video 2) and the dynamics of bundle formation was slower (Extended Data Fig. 1j-l). These results suggest that the initial array of microtubules crosslinked by PRC1 is largely nucleated by the augmin complex.

138 To verify that the redistribution of PRC1 indeed reflects changes of the microtubule
139 network, which was observed in STED images, we first used nocodazole to depolymerize
140 microtubules at the rosette stage. This treatment caused the disappearance of the PRC1 network
141 (Extended Data Fig. 2a), indicating that PRC1 forming this structure is bound to microtubules.
142 Second, we noticed that PRC1 colocalized with microtubules in the central part of the spindle
143 but was excluded from astral microtubules throughout prometaphase (Fig. 1a and Extended
144 Data Fig. 2b), suggesting that PRC1 selectively localizes to antiparallel microtubule overlaps
145 already in early mitosis. Third, we imaged spindles stained with SiR-tubulin and found that,
146 similarly to PRC1, tubulin signal undergoes a change from a nearly uniform to a spotted
147 distribution (Extended Data Fig. 2c,d). Yet, PRC1 is a better marker of antiparallel overlaps
148 not only because of its specificity but also because of the lower background signal (Fig. 1b vs.
149 Extended Data Fig. 2c). Moreover, an increase in the number of bundles during prometaphase
150 was observed in horizontally oriented HeLa spindles labeled with PRC1-GFP, as well as in
151 spindles of human non-transformed retinal pigment epithelial hTERT-RPE1 cells stained with
152 SiR-tubulin (Extended Data Fig. 2e), suggesting that the process of bundle formation is
153 independent of the cell line and labeling. Taken together, these results confirm that the PRC1
154 redistribution reflects the redistribution of overlap microtubules from a nearly uniform network
155 in early prometaphase to the regularly spaced overlap bundles in metaphase.
156

Figure 1

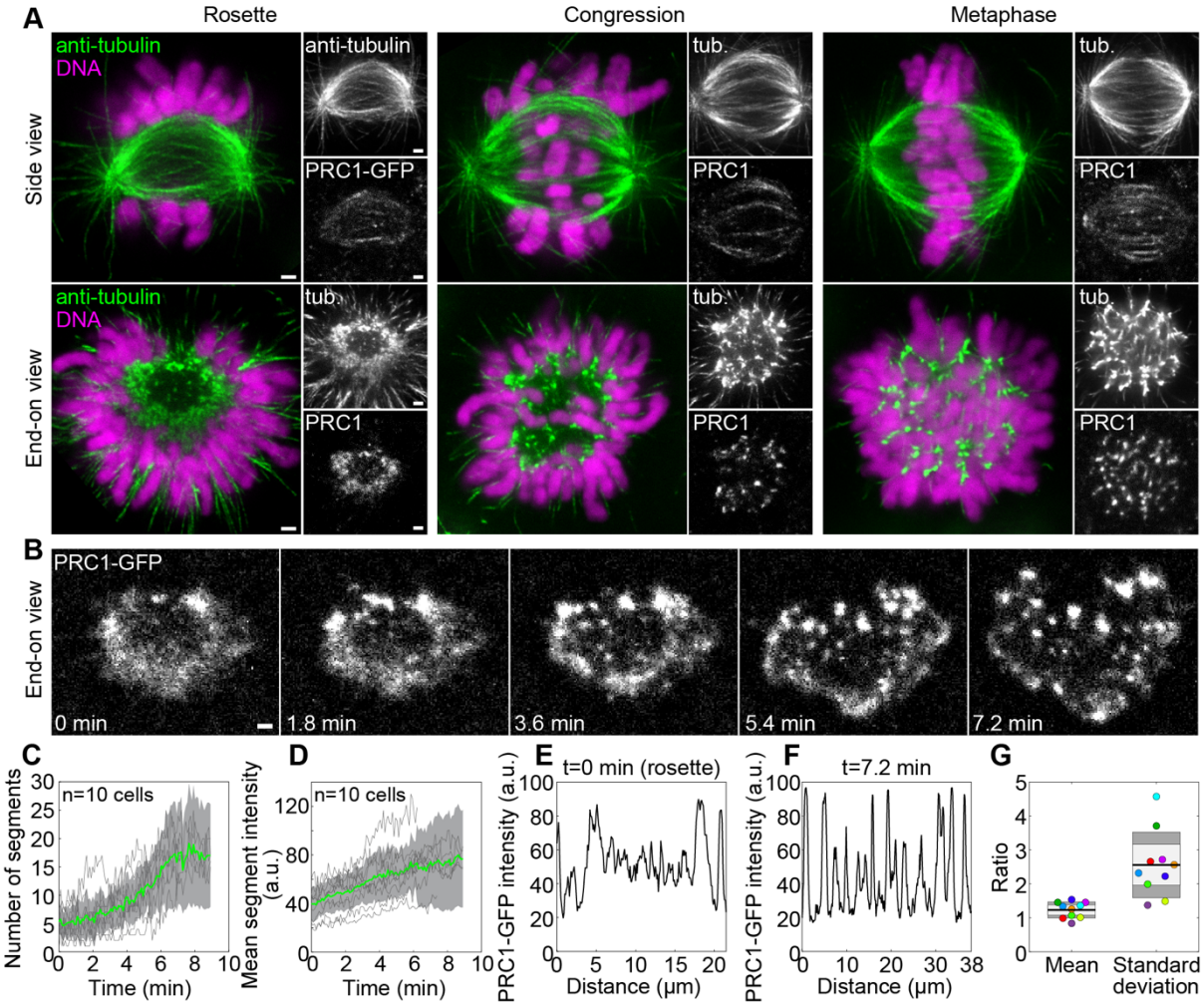

Fig. 1: PRC1-crosslinked microtubules undergo a transition from a loose array to bundles during spindle assembly.

a, Spindles immunostained for α-tubulin and imaged at STED resolution in a HeLa-Kyoto BAC cell line stably expressing PRC1-GFP with DNA stained by DAPI (both imaged at a confocal resolution), in early prometaphase ("Rosette"), late prometaphase ("Congression"), and metaphase. Spindles lying parallel (first row) or perpendicular (second row) to the imaging plane are shown. **b**, Time lapse images (single plane) of a cross-section of a vertically oriented prometaphase spindle in a HeLa-Kyoto BAC cell stably expressing PRC1-GFP, starting with the prometaphase rosette. **c**, Number of PRC1 segments in the midplane over time for cells as in panel **b**, obtained using Squash segmentation. Gray lines represent individual cells, green line the mean and gray areas the standard deviation, n=10 cells in 10 independent experiments. **d**, Mean intensity of PRC1 segments from the same cells as in **c**. **e**,**f**, Intensity line plots of PRC1-GFP in the cell from panel **b** at t=0 (**e**) and t=7.2 min (**f**) along the periphery of the spindle cross-section (lines shown in Extended Data Fig. 1f). **g,** Ratio of mean PRC1-GFP intensity in panels **f** and **e** ("Mean") and ratio of the standard deviation in panels **f** and **e** ("Standard deviation"). The black line shows the mean; the light and dark grey areas mark 95% confidence interval on the mean and

standard deviation, respectively; n=10 cells in 10 independent experiments. Dots of the same color represent the same cells. All scale bars, 1 μm.

Kinetochores promote overlap bundle formation by CENP-E-mediated attachments in an Aurora B-dependent manner

In metaphase, overlap microtubule bundles are found close to a pair of sister kinetochores[53,54]. This finding inspired us to ask whether kinetochores play a role in bundle formation during early prometaphase (Fig. 2a), a stage when kinetochores are laterally attached to spindle microtubules[49,50,55,56]. We found that, in a rosette cross-section of unperturbed spindles, most of the PRC1-labeled bundles had an adjacent kinetochore at its outer side (Fig. 2b). The bundles with an associated kinetochore had a higher PRC1 signal intensity than those without a kinetochore (Fig. 2c), consistent with the hypothesis that kinetochores promote microtubule bundling.

To explore the role of lateral attachments of kinetochores in bundle formation, we inhibited Aurora B, which is in prometaphase localized mainly at centromeres (Extended Data Fig. 3a) and required for the lateral attachment[50,57–59]. We first explored the effect of Aurora B inhibition by barasertib (AZD1152-HQPA)[60,61] on mature bundles in metaphase. Strikingly, we found a 4.2-fold decrease in the signal intensity of individual PRC1-labeled bundles in the cross-section of metaphase spindles (n=452 bundles from 14 cells, Fig. 2d,e; Extended Data Fig. 3b and side view in Extended Data Fig. 3c), suggesting that antiparallel bundles contained fewer microtubules. To confirm this, we measured the tubulin signal intensity in the central part of individual bridging fibers in the region between sister kinetochores in metaphase and found a 7.6-fold decrease upon Aurora B inhibition (Fig. 2f,g and Extended Data Fig. 3d). Thus, Aurora B activity regulates the number of microtubules within the bridging fibers in metaphase.

We addressed the role of Aurora B from another angle by exploring localization relationships between Aurora B and PRC1 in metaphase. We found that the signal intensity of PRC1 within the bridging fiber is correlated with the signal of Aurora B in the neighboring centromere (Extended Data Fig. 3e). Moreover, when we displaced Aurora B from the inner centromere to a position closer to the kinetochore by transfecting cells with CENP-B-INCENP-GFP[62–64], we observed a remarkable change in the PRC1 signal distribution. Instead of a single broad PRC1 peak in the central part of the spindle that is evident in untreated cells, the cells with displaced Aurora B showed two PRC1 peaks about 1 μm away from the spindle equator

207 on either side (Fig. 2h,i and Extended Data Fig. 3f). These results suggest that Aurora B
208 regulates the localization of PRC1-labeled bundles within the spindle.
209 To test the effect of Aurora B on the dynamics of bundle formation during early
210 prometaphase, we combined the bundling assay with acute inhibition of Aurora B by barasertib
211 added at the rosette stage (Fig. 2j and Supplementary Video 3). Aurora B inhibition led to a
212 slower increase in the number and intensity of PRC1-labeled bundles over time in comparison
213 with untreated cells (Extended Data Fig. 3g,h), which confirmed that Aurora B regulates the
214 dynamics of bundle formation.
215

Figure 2

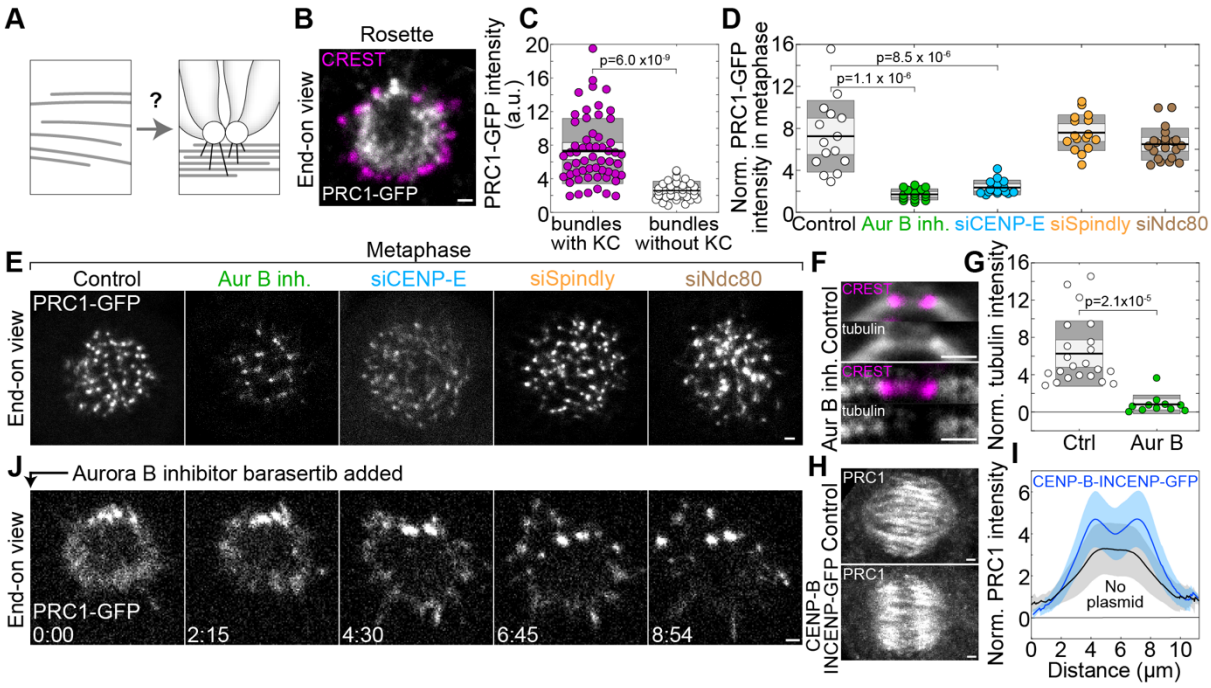

216
217
218 **Fig. 2: Kinetochores promote microtubule bundle formation in an Aurora B-dependent manner.**
219 **a**, Schematic view of kinetochore-driven overlap bundle formation. **b**, Midplane of a vertically oriented
220 prometaphase rosette immunostained for CREST (magenta) in a HeLa-Kyoto BAC cell line stably expressing
221 PRC1-GFP (white). **c**, PRC1-GFP intensity of bundles with and without adjacent kinetochore, n=57 bundles with
222 kinetochores attached and 30 without, in 10 cells from 3 independent immunostainings. **d**, PRC1-GFP intensity
223 of bundles in vertically oriented metaphase spindles, normalized to the cytoplasmic PRC1-GFP intensity. Circles
224 represent the mean bundle intensity per spindle. One-way ANOVA test showed significant difference between
225 group means, p-values are given for the significant differences from control. Numbers of bundles/cells from left
226 to right: 827/15, 452/14, 730/15, 880/16, 774/21; 3 independent experiments per condition. **e**, Images of vertically
227 oriented metaphase spindles in a HeLa-Kyoto BAC cell line stably expressing PRC1-GFP (white), treated as
228 indicated. **f**, Image of a region around a kinetochore pair immunostained for CREST (magenta) and tubulin (white)
229 in an untransfected HeLa cell, control (top) and after Aurora B inhibition (bottom). Merged channels and only

230 tubulin are shown. **g**, Mean tubulin intensity in the middle of the bridging fiber in control and Aurora B-inhibited
231 cells, normalized to the cytoplasmatic anti-tubulin intensity; n=22 bundles from 14 cells for control and 11 bundles
232 from 9 cells for Aurora B inhibition, from 3 independent immunostainings. **h**, Maximum-intensity projections of
233 41 planes of metaphase spindles immunostained for PRC1 (white) in an untransfected HeLa cell line (control, top
234 image), and cells transfected with CENP-B-INCENP-GFP (bottom image). **i**, Line intensity profiles of the anti-
235 PRC1 signal intensity, normalized to the cytoplasmatic anti-PRC1 signal intensity, along the spindle main axis,
236 for control (n=33) and treated cells as in **h** (n=30), mean (central line) and standard deviation (colored surfaces),
237 3 independent experiments per condition. **j**, Time lapse images (single plane) of a cross-section of a vertically
238 oriented prometaphase spindle in a HeLa-Kyoto BAC cell stably expressing PRC1-GFP, after addition of the
239 Aurora B inhibitor Barasertib at the prometaphase rosette stage. In **c**, **d** and **g** the black line shows the mean; the
240 light and dark grey areas mark 95% confidence interval on the mean and standard deviation, respectively. All
241 scale bars, 1 μm.
242
243 The mechanism by which Aurora B at the kinetochore promotes microtubule bundling
244 likely relies on Aurora B substrates involved in microtubule binding. We hypothesize that if
245 microtubule-binding proteins that are localized at the kinetochore in multiple copies attach to
246 several microtubules positioned close to the kinetochore, this could promote microtubule
247 bundling (Fig. 3a). Candidates for this activity are two motor proteins, CENP-E (kinesin-7)
248 and cytoplasmic dynein, and the outer kinetochore protein Ndc80, given that they bind to
249 microtubules, localize at the kinetochore in prometaphase (CENP-E and dynein) or throughout
250 mitosis (Ndc80), and are regulated by Aurora B[50,65–67].
251 We first analyzed the signal intensity of PRC1-labeled bundles in metaphase after
252 depletion of these candidates. CENP-E depletion by siRNA resulted in a 3.1-fold lower
253 intensity of PRC1 in individual bundles in metaphase (n=730 bundles from 14 cells, Fig. 2d,e
254 and Extended Data Fig. 3b,c; see Extended Data Fig. 4 for depletion efficiency) and a 2.8-fold
255 decrease in the tubulin signal intensity in the central part of individual bridging fibers (Fig.
256 3b,c and Extended Data Fig. 3d). These results suggest that CENP-E is required for proper
257 bundle formation and motivated us to explore its localization and dynamics during early
258 prometaphase. In the rosette, we found that CENP-E localizes at the side of the kinetochore
259 facing the PRC1-labeled bundles (Fig. 3d,e), which suggests that it links the kinetochore with
260 the antiparallel bundles. The bundling assay revealed that acute inhibition of CENP-E by GSK-
261 923295[68] at the rosette stage led to a slower increase in the number and intensity of PRC1-
262 labeled bundles over time than in untreated cells (Fig. 3f, Extended Data Fig. 3i,j and
263 Supplementary Video 4), supporting a role of CENP-E in bundle formation. Finally, the
264 hypothesis that CENP-E promotes bundling predicts that overexpression of CENP-E should
265 lead to increased bundling, which we indeed observed as a higher intensity of PRC1-labeled

266 bundles in metaphase upon CENP-E overexpression (Fig. 3g,h and Extended Data Fig. 3k).
267 Taken together, these results indicate that kinetochores promote bundle formation via CENP-
268 E-mediated microtubule binding.

269 To test whether dynein at the kinetochore is required for overlap bundle formation, we
270 depleted Spindly, a kinetochore-specific adaptor for dynein that recruits dynein to the
271 kinetochore[69]. Spindly depletion did not change the signal intensity of PRC1-labeled bundles
272 in metaphase (Fig. 2d,e and Extended Data Fig. 3b; see Extended Data Fig. 4 for depletion
273 efficiency), suggesting that dynein is not crucial for overlap bundle formation. Similarly,
274 Ndc80 depletion did not alter bundle intensity (Fig. 2d,e and Extended Data Fig. 2b; see
275 Extended Data Fig. 4 for depletion efficiency), arguing against a major role of Ndc80 in overlap
276 bundle formation. Moreover, as Ndc80 is required for the establishment of end-on attachments
277 of kinetochores to microtubules and thus the formation of kinetochore fibers[57,66,70,71], these data
278 imply that overlap microtubule bundles can form independently of kinetochore fibers.
279
280

Figure 3

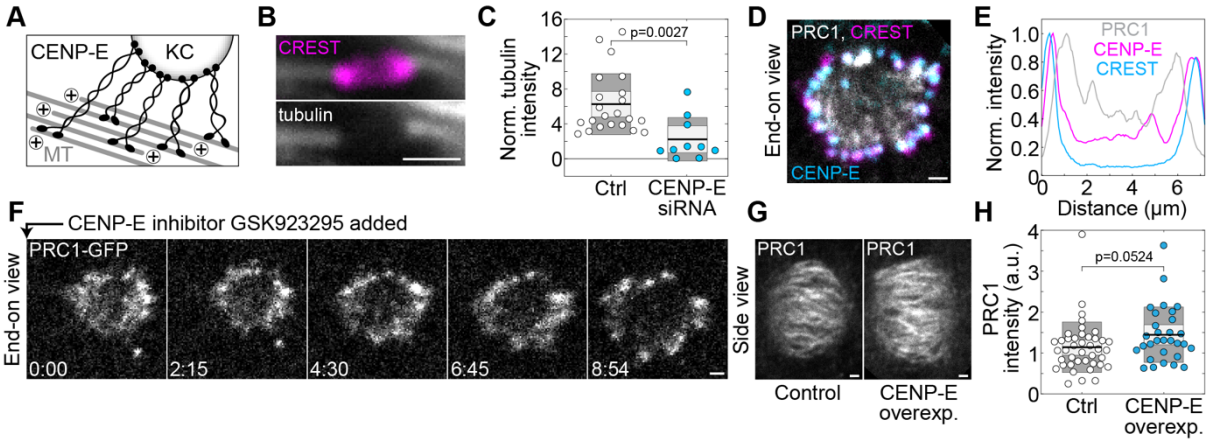

281
282

283 **Fig. 3: CENP-E promotes overlap bundle formation.**

284 **a**, Schematic view of how CENP-E may promote microtubule bundling. **b**, Image of a region close to kinetochores
285 immunostained for CREST (magenta) and tubulin (white) in a CENP-E depleted HeLa cell. **c**, Mean tubulin
286 intensity in the middle of the bridging fiber in control and CENP-E depleted cells, normalized to the cytoplasmatic
287 tubulin intensity, n=22 bundles from 14 cells for control and 10 bundles from 7 cells for CENP-E depletion, from
288 3 independent immunostainings. **d**, Cross-section of a vertically oriented prometaphase rosette immunostained
289 for CREST (magenta) and CENP-E (cyan) in a HeLa-Kyoto BAC cell line stably expressing PRC1-GFP (white).
290 **e**, Line intensity plots of PRC1-GFP, CREST and CENP-E from the spindle shown in **d**, normalized to the
291 corresponding maximum value. The line was drawn across the middle of the spindle cross-section, with a line
292 thickness of 1/3 of the spindle cross-section. **f**, Time lapse images (single plane) of a cross-section of a vertically

293 oriented prometaphase spindle in a HeLa-Kyoto BAC cell stably expressing PRC1-GFP (white), after addition of
294 the CENP-E inhibitor GSK923295 at the prometaphase rosette stage. **g**, Images of horizontally oriented metaphase
295 spindles immunostained for PRC1 (white) in an untransfected HeLa cell line (control, left) and after CENP-E
296 overexpression (right). **h**, Total PRC1 intensity on the spindle in control (n=41) and CENP-E overexpression
297 (n=30), from 3 immunostainings. In **c** and **h**, the black line shows the mean; the light and dark grey areas mark
298 95% confidence interval on the mean and standard deviation, respectively. All scale bars, 1 μm.
299

300 **Steric interactions of the chromosomes separate the bundles and expand spindle width**

301

302 As the bundles form, they undergo characteristic movements. We first focused on the bundles
303 that connect the centrosomes in a straight line, which can be identified by the highest PRC1
304 signal and a lack of an attached chromosome at the rosette stage (see Fig 1a). These bundles
305 are typically found at the edge of the rosette and become centrally positioned over a period of
306 about 5 minutes (Fig. 4a, images to the left). We traced the movement of all bundles and found
307 that, in a coordinate system centered at the brightest bundles, the bundles forming adjacent to
308 them move outwards and encircle them, whereas the bundles forming on the opposite side of
309 the cross-section move away from the brightest bundles (Fig. 4a, traces and Supplementary
310 Video 5). As this movement is accompanied by the arrival of more and more chromosomes to
311 the spindle midplane, we hypothesized that chromosomes promote bundle separation and thus
312 spindle width expansion by steric effects (crowding) upon congression to the midplane. Indeed,
313 we found that as new chromosomes arrived at the midplane, the chromosomes that were already
314 there moved away from the site of the new arrival (Fig. 4b left). This led to the overall outward
315 movement of the PRC1-labeled bundles and spindle widening (Fig. 4b right and Supplementary
316 Video 6). When looking at the spindles in a side view, we found that the spindle width increases
317 as increasingly more chromosomes arrive to the metaphase plate (Fig. 4c,d and Supplementary
318 Video 7). These results support the hypothesis that chromosome crowding increases bundle
319 separation.

320 This hypothesis predicts that removing the chromosomes from the spindle and/or
321 decondensing the chromatin should result in narrower spindles. To test this idea, we induced
322 mitosis with unreplicated genome (MUG) by treating the cells with hydroxyurea to inhibit
323 DNA replication and caffeine to override the DNA damage checkpoint[10,72], because in such
324 cells the bulk of the uncondensed chromatin remains away from the spindle, while the
325 kinetochores are attached to the spindle microtubules[10]. We found that the MUG spindles were
326 significantly narrower with more tightly packed bundles than spindles in untreated cells (Fig.
327 4e,f).

Another prediction of the chromosome crowding hypothesis is that if the chromosomes are not aligned at the equator but distributed over the spindle, the spindles should be narrower, which we tested by several protein depletions. Ndc80 depletion, which results in a large fraction of chromosomes distributed along the spindle due to the absence of kinetochore fibers[70,73,74], led to narrower spindles than in untreated cells (Fig. 4e,f). To test chromosome misalignment without abolishing kinetochore fibers, we used depletion of Kif18A (kinesin-8), a motor protein that regulates chromosome oscillations around the spindle midplane, whose depletion leads to extensive oscillations and hence chromosome scattering along the spindle[75,76]. In this case we also found narrower spindles[77](Fig. 4f). To further test our hypothesis, we divided the cells depleted of CENP-E into two groups: those with high chromosome misalignment, where more than 50% of the total chromosome mass was found away from the spindle midplane, and low misalignment where 1-5 chromosomes were misaligned. CENP-E depleted spindles with high misalignment were narrower than those with low misalignment (Fig. 4e,f). Taken together, these results support the hypothesis that chromosome accumulation on the metaphase plate promotes the separation of the associated microtubule bundles and spindle width expansion.

Figure 4

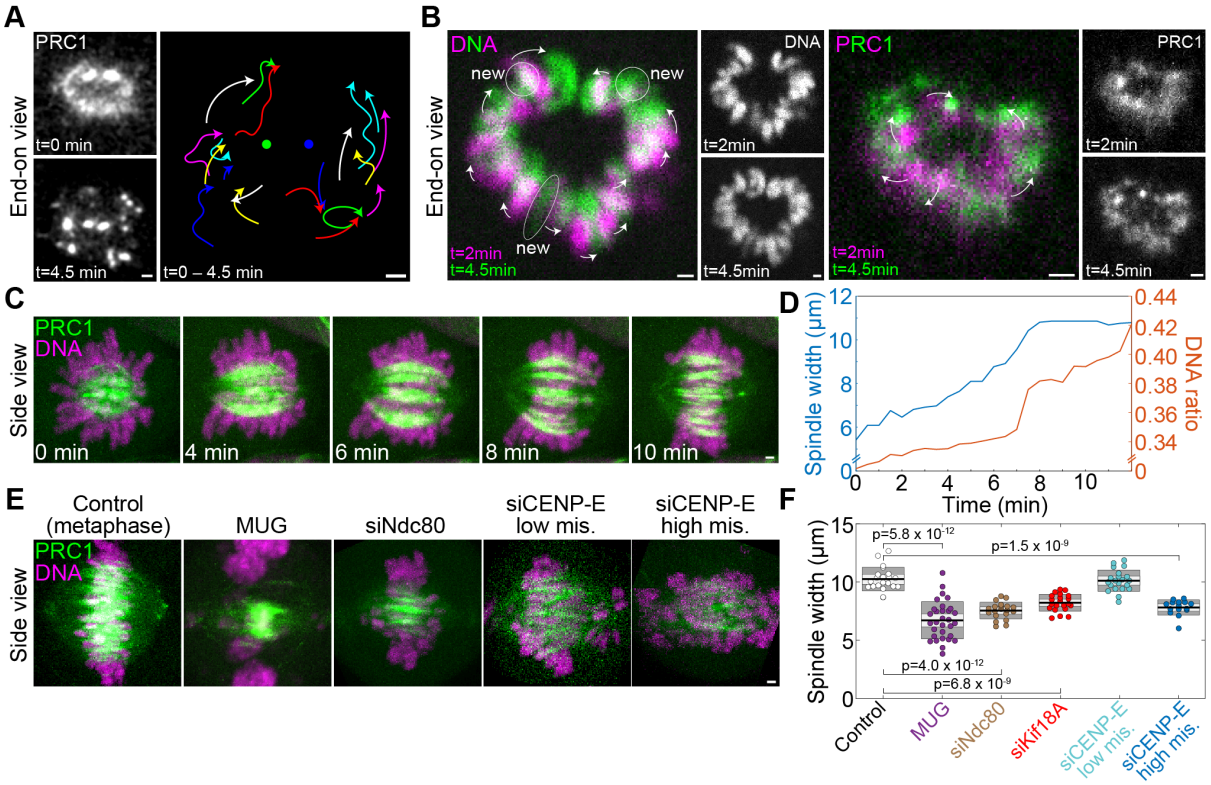

Fig. 4: Chromosomes separate microtubule bundles and increase spindle width.

a, Left, Vertical prometaphase rosette cross-section (single plane) in a HeLa-Kyoto BAC cell stably expressing PRC1-GFP, before (time 0) and after antiparallel bundle formation (4.5 minutes). Right, trajectories of all bundles from time 0 (free end of each curve) until 4.5 minutes (arrowheads), where the points between the end points were smoothed for better visibility and raw data are shown in Supplementary Video 5. Two large bundles visible at the top at time 0 are fixed in space (central points). Time interval between acquired images is 2.7 seconds. **b**, Cross-section of a vertically oriented prometaphase rosette (single plane), showing DNA stained with SiR-DNA dye (left block) or PRC1-GFP (right block), as indicated, in a HeLa-Kyoto BAC cell stably expressing PRC1-GFP, at t=2 min (magenta) and t=4.5 min (green). Individual images are shown in white at the right of the merged images. Encircled areas marked "new" denote the chromosomes that arrived to the spindle midplane between t=2 min and t=4.5 min, arrows denote the movement of DNA (left) or PRC1 bundles (right). **c**, Time-lapse images of a horizontally oriented spindle in a HeLa-Kyoto BAC cell stably expressing PRC1-GFP (green), and DNA stained with SiR-DNA (magenta) starting with early prometaphase. Sum of 41 planes is shown. **d**, Spindle width and proportion of DNA at the metaphase plate over time for the cell shown in **c**. **e**, Live-cell images of metaphase spindles in HeLa-Kyoto BAC cells stably expressing PRC1-GFP (green), and DNA stained with SiR-DNA (magenta), treated as indicated. Maximal projections of 41 planes are shown. **f**, Spindle width for the indicated treatments. The black line shows the mean; the light and dark grey areas mark 95% confidence interval on the mean and standard deviation, respectively. One-way ANOVA test showed significant difference between group means, p-values for significant differences from control are shown. Number of cells was 15-31 per group. Data for Kif18A siRNA are replotted from[77]. All scale bars, 1 μm.

Theoretical model of bundle formation

To understand the physics of bundle formation, we develop a theoretical model that allows us to identify the conditions that lead to the formation of multiple bundles, each bound to a kinetochore. We aim for a minimal model that includes key interactions between microtubules, kinetochores, chromosomes, and crosslinkers. As these interactions are complex, a minimal model is an optimal tool to understand the interplay between these multiple components and their roles in bundle formation, and to strengthen the hypotheses by comparison with experiments.

In our one-dimensional approach, representing the rim of the spindle midplane, we describe kinetochores as discrete points and explore the spatial distribution of microtubules (Fig. 5a). Kinetochores are considered as attractive points for microtubules, where multiple microtubules can bind and form a bundle. Microtubules experience mutual local attraction due to crosslinkers and inter-microtubule repulsion due to excluded volume effects. Finally, steric interactions between chromosomes and microtubules are described as a nonlocal inter-microtubule repulsion. A description of the model is given in Methods.

384 The solutions of the model show that kinetochores play an important role in the
385 formation of microtubule bundles, with peaks of microtubule density at their positions (Fig.
386 5b). These peaks increase for an increasing kinetochore-microtubule attraction, which is
387 accompanied by a decrease of the microtubule density between the kinetochores. A decrease
388 in this attraction leads to an almost homogeneous microtubule distribution. A similar behavior
389 was observed in experiments, where depletion of CENP-E led to thinner bundles and its
390 overexpression to thicker bundles (Fig. 2d and Fig. 3g,h). Thus, theory together with
391 experiments suggest that microtubules respond to the kinetochore-microtubule attraction by
392 rearranging themselves between a uniform distribution and pronounced bundles at
393 kinetochores.
394 Even though kinetochores are major attraction sites, microtubule crosslinkers also
395 affect the formation of bundles (Fig. 5c). An increase in the crosslinker concentration leads to
396 more pronounced bundles at the kinetochores, showing a similar trend as the increase in
397 kinetochore-microtubule attraction. In agreement with this theoretical result, experiments in
398 which PRC1 was overexpressed showed excessively thick overlap microtubule bundles (Fig.
399 5d and Extended Data Fig. 5). Thus, microtubule crosslinkers act cooperatively with
400 kinetochores in the formation of bundles.
401 Finally, we explored how the distance between kinetochores influences microtubule
402 distributions. When we increased the distance, the bundles at the kinetochores remained the
403 same, whereas the distribution of the microtubules between the kinetochores became
404 predominantly uniform, with more microtubules at the midpoint than for smaller inter-
405 kinetochore distance (Fig. 5e). We assume that the cases with larger and smaller distances
406 correspond to the transition of the spindle from prometaphase to metaphase, because during
407 this transition increasingly more kinetochores arrive to the spindle midplane and thus their
408 distance decreases. Indeed, we observed in experiments that in early prometaphase the
409 microtubule distribution was roughly uniform, whereas at a later phase deeper valleys between
410 the peaks appeared (Fig. 1e,f). Taken together, these results support our main hypothesis that
411 the attractive interactions due to kinetochores and crosslinkers drive the formation of
412 microtubule bundles.
413

Figure 5

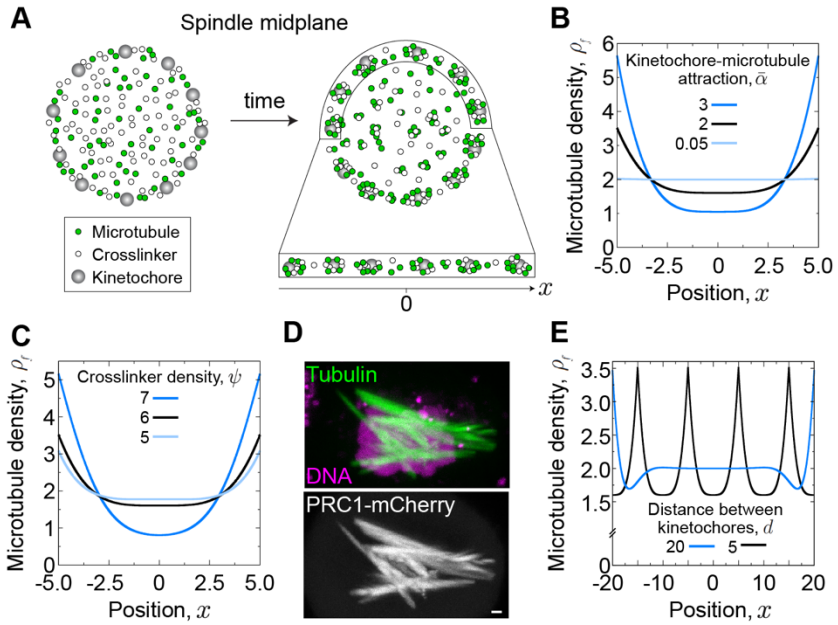

Fig. 5: Theoretical model of bundle formation.

a, Schematic representation of the model. Kinetochores (grey) are equally spaced along the edge of the spindle midplane. Microtubules (green) and crosslinkers (white) are initially uniformly distributed and gather into bundles over time. **b**, Steady-state microtubule density, ρ_f, for 3 values of the kinetochore-microtubule attraction, $\bar{\alpha}$, as indicated. Other parameters are: $\psi = 6, d = 5, \rho_b = 2, \kappa = 5$ (all parameters are dimensionless, see Methods). The kinetochores are positioned at $x = \pm d$. **c**, Steady-state microtubule density, ρ_f, for 3 values of the crosslinker density, ψ, as indicated; $\bar{\alpha} = 2, d = 5, \rho_b = 2, \kappa = 5$. **d**, Spindle in a HeLa-TDS cell with overexpressed PRC1. Top: microtubules (SiR-tubulin, green) and DNA (Hoechst 33342, magenta), bottom: PRC1-mCherry (white). Scale bar, 1 µm. **e**, Steady-state microtubule density, ρ_f, for 2 values of the distance between kinetochores, d, as indicated; $\bar{\alpha} = 2, \psi = 6, \rho_b = 2, \kappa = 5$.

Functional role of PRC1-labeled bundles in chromosome segregation fidelity

Finally, we addressed the role of overlap bundles in chromosome segregation fidelity. It has been shown that in prometaphase microtubules adjacent to the centromeres stimulate kinetochore phosphorylation and thus correction of erroneous kinetochore-microtubule attachments through microtubule binding of Borealin, a component of the Chromosome Passenger Complex[71]. We hypothesized that PRC1-bound overlap bundles are required for error correction, in a manner that Aurora B not only promotes the formation of these bundles (Fig. 2), but also uses them as tracks for the movement towards kinetochore targets to correct the wrong attachments (Fig. 6a). This hypothesis predicts that reduction of overlap

437 microtubules should lead to a decrease in outer kinetochore phosphorylation and an increase in
438 chromosome segregation errors.

439 To test these predictions, we reduced the overlap bundles by depleting PRC1, as this is
440 the most specific way to reduce these bundles known so far, which reduces overlap bundle
441 microtubules by about 50% without affecting kinetochore fibers[22]. We checked the
442 phosphorylation of serine 7 (Ser7) of CENP-A, a known Aurora B substrate[78], and found a
443 significant drop in phosphorylation after PRC1 depletion (Fig. 6b,c), which suggests that
444 PRC1-crosslinked overlap microtubules promote kinetochore phosphorylation.

445 To assess the role of overlap bundles in chromosome segregation fidelity, we first
446 analyzed lagging kinetochores in anaphase and found that PRC1 depletion caused a small
447 increase in lagging kinetochores over control cells, from 1% to 3.5% (Fig. 6d,f; see Extended
448 Data Fig. 4 for depletion efficiency)[22]. To directly examine the function of overlap bundles in
449 the correction of incorrect kinetochore attachments, we treated the cells with monastrol to block
450 the spindles in a monopolar state with high incidence of syntelic attachments, where both sister
451 kinetochores are attached to the same spindle pole[15], and washed out monastrol after 40-60
452 minutes to allow for spindle assembly (Fig. 6d). Immunofluorescence analysis of spindles in
453 anaphase showed that monastrol-treated cells that were not depleted of PRC1 had only 2.3%
454 (Fig. 6f), indicating that error correction operates in cells with proper overlap bundles. In
455 contrast, monastrol-treated cells that were depleted of PRC1 had a significantly higher
456 incidence of lagging kinetochores, 10.8% (Fig. 6e,f), revealing a role of overlap bundles in
457 error correction. Taken together, these results suggest that PRC1-bound overlap bundles have
458 a function in correcting erroneous kinetochore-microtubule attachments by promoting Aurora
459 B-driven kinetochore phosphorylation.
460

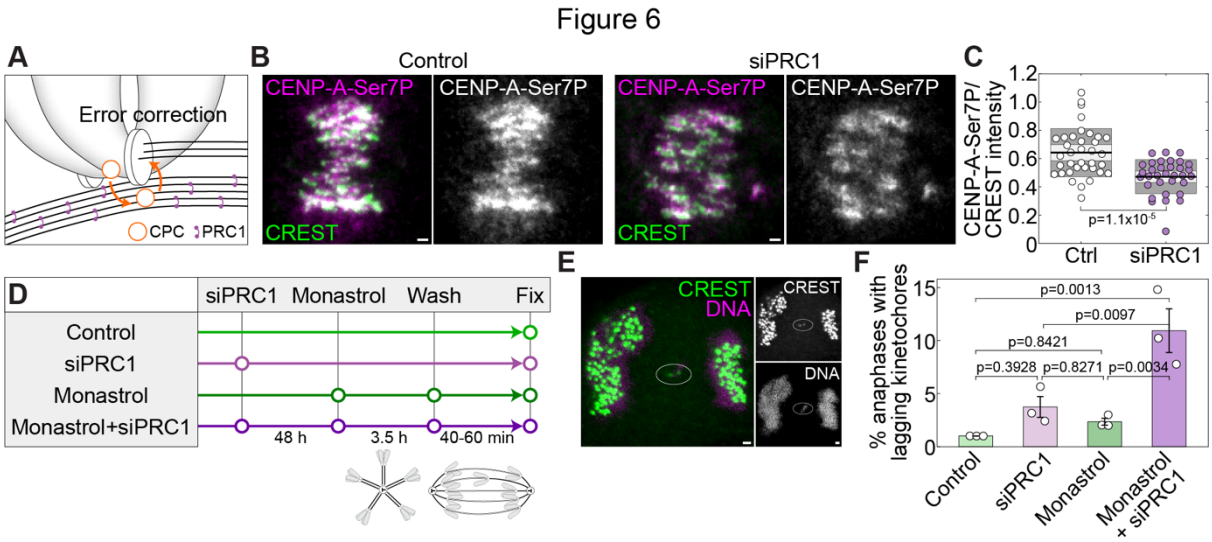

Fig. 6: PRC1-bound overlap bundles promote chromosome segregation fidelity.
a, Scheme depicting the hypothesis that antiparallel overlaps help Aurora B to reach the kinetochore components, phosphorylate them and correct erroneous attachments. **b**, Images showing anti-CENP-A-Ser7P (magenta) and CREST (green) in control (left) and PRC1-depleted HeLa cells (right), merged channels and only anti-CENP-A-Ser7P in white are shown. **c**, Ratio between anti-CENP-A-Ser7P and CREST in control (n=36) and PRC1-depleted cells (n=33), from 3 immunostaining experiments. **d**, Scheme of the protocol in which monastrol washout is used to increases erroneous attachments in prometaphase. **e**, Lagging chromosome (encircled) in anaphase in a PRC1-depleted HeLa cell after monastrol washout. Left, merged image of CREST (green) and DNA (magenta). Right, individual channels (white). **f**, Frequency of lagging kinetochores in control (3 anaphases with lagging kinetochores / 299 total anaphases), PRC1 siRNA (8/231), monastrol washout (7/298), and PRC1siRNA+monatrol washout (28/259) from 3 immunostaining experiments per condition. One-way ANOVA test showed significant difference between group means, p-values are shown. The cell line used in this figure was unlabeled HeLa-TDS. All scale bars, 1 µm.

DISCUSSION

Kinetochore- and chromosome-driven transition from a dilute microtubule array to bundles

By combining STED microscopy, a live-cell bundling assay and theory, we have shown that spindle assembly occurs through a transition in which the initially uniform microtubule array is remodeled into bundles (Fig. 7a-c). Our experiments suggest that the temporal evolution of the bundles starts with the initial dilute network of antiparallel overlaps connecting the spindle poles, which relies on augmin-mediated microtubule nucleation together with the crosslinking

488 activity of PRC1 and possibly other crosslinkers. When a kinetochore simultaneously attaches
489 to the wall of several of these microtubules via CENP-E, this promotes further bundling of
490 increasingly more microtubules by crosslinkers. While the chromosomes progressively
491 congress to the spindle equator, they crowd there and thus move together with the attached
492 bundles away from each other within the equatorial plane. As a result, the spindle cross-section
493 widens and becomes uniformly filled with bundles and the attached chromosomes, and the
494 spindle attains its metaphase shape.

495 We propose several competing mechanisms that are in action during transition to
496 bundles. There are two attractive and two repulsive effects between the microtubules.
497 Microtubules get attracted to neighboring microtubules via the crosslinkers (Fig. 7a). This
498 process is facilitated locally by kinetochores because they attach to several adjacent
499 microtubules, which brings the microtubules close to one another and promotes their bundling
500 by crosslinkers (Fig. 7a). Microtubules experience local repulsion from neighbors due to
501 excluded volume effects, and a non-local repulsion due to chromosomes whose crowding at
502 the spindle midplane moves the attached bundles away from each other (Fig. 7b). This non-
503 local repulsion helps to prevent all bundles from ending up as a single thick bundle. A bundling
504 phase transition has been studied in theoretical models of cytoskeleton networks[79,80], but here
505 we show that additional interactions such as those between microtubules and kinetochores are
506 important because they promote bundling. Yet, given that our model is one-dimensional,
507 extensions of the model that would include inter-microtubule orientation may bring about new
508 features of bundle formation.

509

510 **Kinetochores promote overlap bundle formation**

511

512 Our experiments revealed that kinetochores actively promote the formation of antiparallel
513 bundles in prometaphase. Kinetochores have been previously implicated in the formation of
514 antiparallel bundles in different contexts, for example during meiosis I in mouse oocytes, where
515 PRC1 is localized to the kinetochore through interaction with Ndc80, and facilitates bundling
516 of antiparallel overlaps in vicinity of the kinetochore[81]. As we did not find PRC1 at the
517 kinetochore in human somatic cells, the molecular mechanism of bundle formation may differ
518 in these two systems, thought the biophysical mechanisms may be similar. In anaphase in *C.*
519 *elegans* zygotes, formation of antiparallel bundles of the central spindle requires the
520 kinetochore proteins KNL-1, BUB-1, CENP-F, and CLASP[82]. CENP-E, which we identified
521 to be important for microtubule bundling in prometaphase, is also present in the central spindle

522 in anaphase, with an increased bundling activity[83,84]. Thus, it would be interesting to explore
523 the relationship between the kinetochore-related mechanisms that promote the formation of
524 microtubule bundles in prometaphase and anaphase, as well as their evolutionary aspects
525 through comparison between different organisms.
526 We found a role of CENP-E, but not of Ndc80 and dynein, in overlap bundle formation.
527 CENP-E, which is located in the fibrous corona connecting kinetochores to microtubules[67], is
528 a very long and flexible molecule with a contour length of 230 nm[85]. This may allow multiple
529 CENP-E motors at an individual kinetochore to capture and bind laterally to several nearby
530 microtubules. In contrast, Ndc80 complex and cytoplasmic dynein are only 60 and 50 nm long
531 when extended, respectively[86,87]. This difference in length may explain the importance of
532 CENP-E in microtubule bundling, even though this it is not required for lateral attachment[88].
533 Given that CENP-E interacts with PRC1[83], their interaction may also be important for
534 microtubule bundling. In addition to PRC1, other proteins that bind to antiparallel
535 microtubules, such as Eg5, likely assist bundle formation. PRC1-interacting partners Kif4A
536 and MKLP1 may also play a role, similarly to their roles in anaphase[27]. These hypotheses
537 remain to be explored in future studies.
538
539 **Chromosomes separate the bundles and determine the spindle shape**
540
541 Bundling of microtubules by crosslinkers could in principle lead to bundling of most spindle
542 microtubules into a single thick bundle. This is, however, not observed in animal spindles. In
543 contrast, yeast spindles consist of a single microtubule bundle, which is likely due to a smaller
544 number of microtubules, 40 in yeast versus 6000 in human spindles, and shorter spindles that
545 prevent microtubule bending, 1.5 μm long in yeast versus 10 μm in human cells[38,89]. We
546 propose that in animal spindles chromosomes crowding at the metaphase plate, together with
547 coupling the bundle with kinetochore during its formation, promotes bundle separation by
548 driving outward movements of the bundles, which results in spindle widening. Several lines of
549 evidence from our work support this notion. During prometaphase, as more and more
550 chromosomes arrive at the spindle midplane and fill it, the spindle gets progressively wider. In
551 agreement with this, spindles with perturbed chromosome alignment, where chromosome
552 arrangement resembles more the prometaphase state rather than metaphase, are narrower.
553 Examples studied here include depletion of Ndc80, Kif18A, and CENP-E, which have different
554 mechanistic origin of chromosome misalignment[74,75]. Thus, it is unlikely that the observed
555 spindle narrowing is due to perturbation of specific functions of these proteins, but rather due

556 to misalignment itself. Another argument comes from mitosis with unreplicated genome, in
557 which kinetochores interact with spindle microtubules but the DNA is dispersed throughout
558 the cells[10]. As expected, this resulted in narrow spindles, but fully formed bundles due to the
559 presence of kinetochores.
560 Previous work has shown that in HeLa cells, which have a variable number of
561 chromosomes[90], spindle width increases with the number of chromosomes[53]. This result also
562 supports the chromosome crowding hypothesis. Finally, a striking example comes from the
563 finding that a single microtubule bundle connects the spindle poles with chromosomes lying
564 along the sides upon expression of a kinase-inactive Aurora B[91], in agreement with our
565 hypothesis.
566
567 **PRC1-linked overlap microtubules promote chromosome segregation fidelity**
568
569 We have shown that PRC1-bound overlap bundles are required for the correction of synthelic
570 kinetochore-microtubule attachments after spindle assembly from a monopole state. PRC1
571 depletion, which reduces the number of microtubules in the overalp bundles, resulted not only
572 in an increase in lagging kinetochores, but also in decreased kinetochore phosphorylation. By
573 combing these results with a previous work showing that Borealin binding to microtubules
574 stimulates kinetochore phosphorylation and correction of erroneous kinetochore-microtubule
575 attachments[71], we propose that Aurora B, being part of the Chromosome Passenger Complex
576 together with Borealin, not only promotes the formation of PRC1-linked overlap bundles, but
577 also uses them as tracks for the movement towards kinetochores to correct the wrong
578 attachments. The molecular details of this PRC1-based error-correction mechanism remain an
579 exciting topic for future studies.
580 In conclusion, our results reveal that a transition of microtubules from a loose array to
581 bundles, dependent on kinetochores that serve as attraction sites and chromosomes that provide
582 repulsion, promotes spindle assembly. In a broader sense, our study reveals general principles
583 of organization of cytoskeletal filaments. The concepts of attraction sites as drivers of bundle
584 formation may be relevant in other contexts, for example in the formation of actin bundles,
585 where adherens junctions and focal adhesions may act as such sites. Overall, we expect that
586 mechanisms similar to the ones identified here, though with different molecular players, act in
587 a variety of cytoskeletal systems to generate specific filament arrangements required for their
588 function.
589

Figure 7

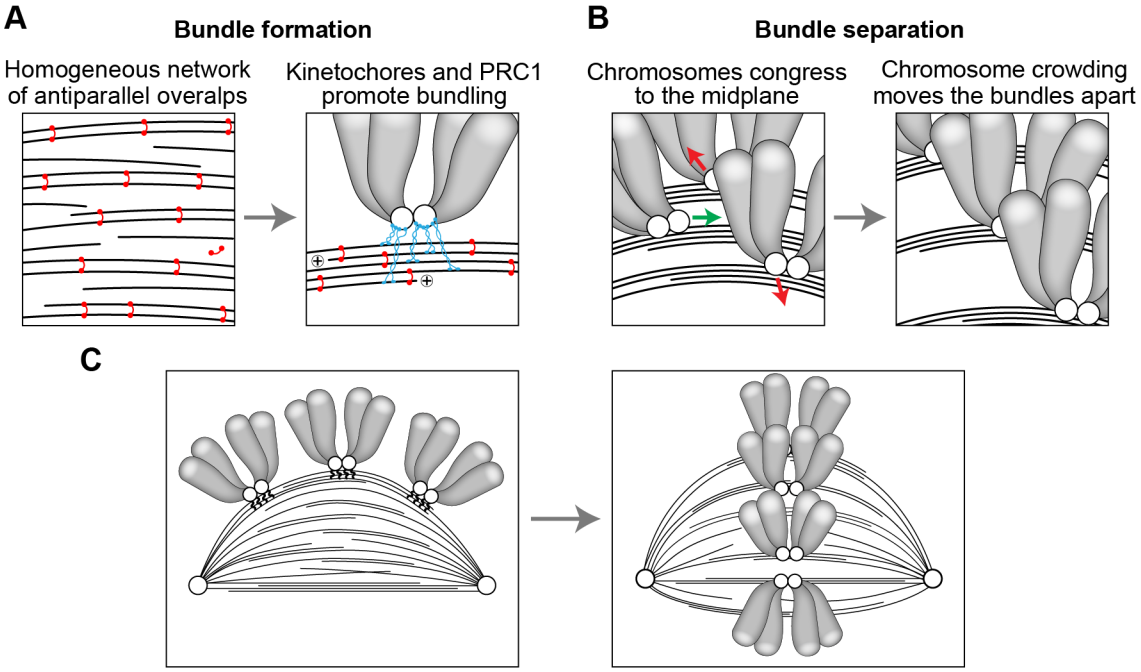

Fig. 7: Model for kinetochore driven overlap formation.

a, A loose microtubule network consisting of uniformly distributed antiparallel overlaps linked by PRC1 (red) undergoes a transition to tight bundles due to the microtubule-binding activity of kinetochores (CENP-E, blue). **b**, Bundles are separated (red arrows) during chromosome congression (green arrow) to the spindle midplane and steric effects of neighboring chromosome arms. **c**, The processes depicted in **a** and **b** lead to a transition from the prometaphase rosette (left), with a loose network of microtubules and laterally attached chromosomes, to a more mature spindle in late prometaphase (right), with distinct and separated bundles.

601 **REFERENCES**
602

603 1. Prosser, S. L. & Pelletier, L. Mitotic spindle assembly in animal cells: A fine balancing
604 act. *Nat. Rev. Mol. Cell Biol.* **18**, 187–201 (2017).
605 2. McIntosh, J. R., Molodtsov, M. I. & Ataullakhanov, F. I. Biophysics of mitosis. *Q.*
606 *Rev. Biophys.* **45**, 147–207 (2012).
607 3. Pavin, N. & Tolić, I. M. Self-Organization and Forces in the Mitotic Spindle. *Annu.*
608 *Rev. Biophys.* **45**, 279–298 (2016).
609 4. McDonald, K. L., O'Toole, E. T., Mastronarde, D. N. & McIntosh, J. R. Kinetochore
610 microtubules in PTK cells. *J. Cell Biol.* **118**, 369–383 (1992).
611 5. Cheeseman, I. M. & Desai, A. Molecular architecture of the kinetochore-microtubule
612 interface. *Nat. Rev. Mol. Cell Biol.* **9**, 33–46 (2008).
613 6. Mastronarde, D. N., McDonald, K. L., Ding, R. & McIntosh, J. R. Interpolar spindle
614 microtubules in PTK cells. *J. Cell Biol.* **123**, 1475–1489 (1993).
615 7. Mitchison, T. J. & Kirschner, M. W. Properties of the Kinetochore In Vitro. I.
616 Microtubule nucleation and tubulin binding. *J. Cell Biol.* **101**, 755–765 (1985).
617 8. Rieder, C. L. & Alexander, S. P. Kinetochores are transported poleward along a single
618 astral microtubule during chromosome attachment to the spindle in newt lung cells. *J.*
619 *Cell Biol.* **110**, 81–95 (1990).
620 9. Wollman, R. *et al.* Efficient chromosome capture requires a bias in the 'search-and-
621 capture' process during mitotic-spindle assembly. *Curr. Biol.* **15**, 828–832 (2005).
622 10. O'Connell, C. B., Lončarek, J., Kaláb, P. & Khodjakov, A. Relative contributions of
623 chromatin and kinetochores to mitotic spindle assembly. *J. Cell Biol.* **187**, 43–51
624 (2009).
625 11. Sikirzhytski, V. *et al.* Microtubules assemble near most kinetochores during early
626 prometaphase in human cells. *J. Cell Biol.* **217**, 2647–2659 (2018).
627 12. Renda, F. *et al.* Non-centrosomal microtubules at kinetochores promote rapid
628 chromosome biorientation during mitosis in human cells. *Curr. Biol.* **in press**, (2022).
629 13. Sawin, K. E., Leguellec, K., Philippe, M. & Mitchison, T. J. Mitotic spindle
630 organization by a plus-end-directed microtubule motor. *Nature* **359**, 540–543 (1992).
631 14. Kapitein, L. C. *et al.* The bipolar mitotic kinesin Eg5 moves on both microtubules that
632 it crosslinks. *Nature* **435**, (2005).
633 15. Kapoor, T. M., Mayer, T. U., Coughlin, M. L. & Mitchison, T. J. Probing spindle
634 assembly mechanisms with monastrol, a small molecule inhibitor of the mitotic
635 kinesin, Eg5. *J. Cell Biol.* **150**, (2000).
636 16. Blangy, A. *et al.* Phosphorylation by p34cdc2 regulates spindle association of human
637 Eg5, a kinesin-related motor essential for bipolar spindle formation in vivo. *Cell* **83**,
638 1159–1169 (1995).
639 17. Kajtez, J. *et al.* Overlap microtubules link sister k-fibres and balance the forces on bi-
640 oriented kinetochores. *Nat. Commun.* **7**, (2016).
641 18. Milas, A. & Tolić, I. Relaxation of interkinetochore tension after severing of a k-fiber
642 depends on the length of the k-fiber stub. *Matters Sel.* (2016)
643 doi:10.19185/matters.201603000025.
644 19. Elting, M. W., Prakash, M., Udy, D. B. & Dumont, S. Mapping Load-Bearing in the
645 Mammalian Spindle Reveals Local Kinetochore Fiber Anchorage that Provides
646 Mechanical Isolation and Redundancy. *Curr. Biol.* **27**, 2112-2122.e5 (2017).
647 20. Maiato, H., Gomes, A. M., Sousa, F. & Barisic, M. Mechanisms of chromosome
648 congression during mitosis. *Biology (Basel).* **6**, 1–56 (2017).
649 21. Suresh, P., Long, A. F. & Dumont, S. Microneedle manipulation of the mammalian
650 spindle reveals specialized, short-lived reinforcement near chromosomes. *Elife* **9**, 1–22

(2020).
22. Jagrić, M., Risteski, P., Martinčić, J., Milas, A. & Tolić, I. M. Optogenetic control of prc1 reveals its role in chromosome alignment on the spindle by overlap length-dependent forces. *Elife* **10**, 1–79 (2021).
23. Risteski, P. *et al.* Coordinated poleward flux of sister kinetochore fibers drives chromosome alignment. *bioRxiv* 2020.12.30.424837 (2021) doi:10.1101/2020.12.30.424837.
24. Brust-Mascher, I., Civelekoglu-Scholey, G., Kwon, M., Mogilner, A. & Scholey, J. M. Model for anaphase B: Role of three mitotic motors in a switch from poleward flux to spindle elongation. *Proc. Natl. Acad. Sci. U. S. A.* **101**, 15938–15943 (2004).
25. Brust-Mascher, I., Sommi, P., Cheerambathur, D. K. & Scholey, J. M. Kinesin-5–dependent Poleward Flux and Spindle Length Control in Drosophila Embryo Mitosis. *Mol. Biol. Cell* **20**, 1749–1762 (2009).
26. Vukušić, K. *et al.* Microtubule Sliding within the Bridging Fiber Pushes Kinetochore Fibers Apart to Segregate Chromosomes. *Dev. Cell* **43**, 11-23.e6 (2017).
27. Vukušić, K., Ponjavić, I., Buđa, R., Risteski, P. & Tolić, I. M. Microtubule-sliding modules based on kinesins EG5 and PRC1-dependent KIF4A drive human spindle elongation. *Dev. Cell* **56**, 1253-1267.e10 (2021).
28. Yu, C. H. *et al.* Central-spindle microtubules are strongly coupled to chromosomes during both anaphase A and anaphase B. *Mol. Biol. Cell* **30**, 2503–2514 (2019).
29. Asthana, J., Cade, N. I., Normanno, D., Lim, W. M. & Surrey, T. Gradual compaction of the central spindle decreases its dynamicity in PRC1 and EB1 gene-edited cells. *Life Sci. Alliance* **4**, (2021).
30. Janson, M. E. *et al.* Crosslinkers and Motors Organize Dynamic Microtubules to Form Stable Bipolar Arrays in Fission Yeast. *Cell* **128**, 357–368 (2007).
31. Kapitein, L. C. *et al.* Microtubule-Driven Multimerization Recruits ase1p onto Overlapping Microtubules. *Curr. Biol.* **18**, 1713–1717 (2008).
32. Subramanian, R. *et al.* Insights into antiparallel microtubule crosslinking by PRC1, a conserved nonmotor microtubule binding protein. *Cell* **142**, 433–443 (2010).
33. Bieling, P., Telley, I. A. & Surrey, T. A minimal midzone protein module controls formation and length of antiparallel microtubule overlaps. *Cell* **142**, 420–432 (2010).
34. Edelmaier, C. J. *et al.* Mechanisms of chromosome biorientation and bipolar spindle assembly analyzed by computational modeling. *Elife* **9**, (2020).
35. Blackwell, R. *et al.* Physical determinants of bipolar mitotic spindle assembly and stability in fission yeast. *Sci. Adv.* **3**, (2017).
36. Winters, L. *et al.* Pivoting of microtubules driven by minus-end-directed motors leads to spindle assembly. *BMC Biol.* **17**, (2019).
37. Nédélec, F. Computer simulations reveal motor properties generating stable antiparallel microtubule interactions. *J. Cell Biol.* **158**, (2002).
38. Kiewisz, R., Fabig, G., Conway, W., Needleman, D. & Müller-Reichert, T. Three-dimensional structure of the kinetochore-fibers in human mitotic spindles. *bioRxiv* 2021.11.13.468347 (2021).
39. Needleman, D. & Dogic, Z. Active matter at the interface between materials science and cell biology. *Nat. Rev. Mater.* **2**, 17048 (2017).
40. Roostalu, J., Rickman, J., Thomas, C., Nédélec, F. & Surrey, T. Determinants of Polar versus Nematic Organization in Networks of Dynamic Microtubules and Mitotic Motors. *Cell* **175**, (2018).
41. Wu, K. T. *et al.* Transition from turbulent to coherent flows in confined three-dimensional active fluids. *Science* **355**, (2017).
42. Hitt, A. L., Cross, A. R. & Williams, R. C. Microtubule solutions display nematic

701 liquid crystalline structure. *J. Biol. Chem.* **265**, 1639–1647 (1990).
702 43. Kierfeld, J., Kühne, T. & Lipowsky, R. Discontinuous unbinding transitions of
703 filament bundles. *Phys. Rev. Lett.* **95**, 1–4 (2005).
704 44. Huisman, B. A. H., Bolhuis, P. G. & Fasolino, A. Phase transition to bundles of
705 flexible supramolecular polymers. *Phys. Rev. Lett.* **100**, (2008).
706 45. Borukhov, I., Bruinsma, R. F., Gelbart, W. M. & Liu, A. J. Structural polymorphism of
707 the cytoskeleton: A model of linker-assisted filament aggregation. *Proc. Natl. Acad.*
708 *Sci. U. S. A.* **102**, (2005).
709 46. Kachan, D., Müller, K. W., Wall, W. A. & Levine, A. J. Discontinuous bundling
710 transition in semiflexible polymer networks induced by Casimir interactions. *Phys.*
711 *Rev. E* **94**, (2016).
712 47. Maxian, O., Donev, A. & Mogilner, A. Interplay between Brownian motion and cross-
713 linking kinetics controls bundling dynamics in actin networks. *bioRxiv*
714 2021.09.17.460819 (2021) doi:https://doi.org/10.1101/2021.09.17.460819.
715 48. Huang, B., Babcock, H. & Zhuang, X. Breaking the diffraction barrier: Super-
716 resolution imaging of cells. *Cell* **143**, 1047–1058 (2010).
717 49. Bolzer, A. *et al.* Three-dimensional maps of all chromosomes in human male
718 fibroblast nuclei and prometaphase rosettes. *PLoS Biol.* **3**, 0826–0842 (2005).
719 50. Itoh, G. *et al.* Lateral attachment of kinetochores to microtubules is enriched in
720 prometaphase rosette and facilitates chromosome alignment and bi-orientation
721 establishment. *Sci. Rep.* **8**, 1–18 (2018).
722 51. Goshima, G., Mayer, M., Zhang, N., Stuurman, N. & Vale, R. D. Augmin: A protein
723 complex required for centrosome-independent microtubule generation within the
724 spindle. *J. Cell Biol.* **181**, 421–429 (2008).
725 52. Uehara, R. *et al.* The augmin complex plays a critical role in spindle microtubule
726 generation for mitotic progression and cytokinesis in human cells. *Proc. Natl. Acad.*
727 *Sci. U. S. A.* **106**, 6998–7003 (2009).
728 53. Polak, B., Risteski, P., Lesjak, S. & Tolić, I. M. PRC 1-labeled microtubule bundles
729 and kinetochore pairs show one-to-one association in metaphase. *EMBO Rep.* **18**, 217–
730 230 (2017).
731 54. O'Toole, E., Morphew, M. & Richard McIntosh, J. Electron tomography reveals
732 aspects of spindle structure important for mechanical stability at metaphase. *Mol. Biol.*
733 *Cell* **31**, 184–195 (2020).
734 55. Nagele, R., Freeman, T., Mcmorrow, L. & Lee, H. Precise spatial positioning of
735 chromosomes during prometaphase: evidence for chromosomal order. *Science* **270**,
736 1831–1835 (1995).
737 56. Chaly, N. & Brown, D. L. The prometaphase configuration and chromosome order in
738 early mitosis. *J. Cell Sci.* **91**, 325–335 (1988).
739 57. DeLuca, J. G. *et al.* Kinetochore Microtubule Dynamics and Attachment Stability Are
740 Regulated by Hec1. *Cell* **127**, 969–982 (2006).
741 58. Welburn, J. P. I. *et al.* Aurora B Phosphorylates Spatially Distinct Targets to
742 Differentially Regulate the Kinetochore-Microtubule Interface. *Mol. Cell* **38**, 383–392
743 (2010).
744 59. Shrestha, R. L. *et al.* Aurora-B kinase pathway controls the lateral to end-on
745 conversion of kinetochore-microtubule attachments in human cells. *Nat. Commun.* **8**,
746 1–12 (2017).
747 60. Mortlock, A. A. *et al.* Discovery, synthesis, and in vivo activity of a new class of
748 pyrazoloquinazolines as selective inhibitors of aurora B kinase. *J. Med. Chem.* **50**,
749 2213–2224 (2007).
750 61. Dennis, M. *et al.* Phase i study of the Aurora B kinase inhibitor barasertib (AZD1152)

751 to assess the pharmacokinetics, metabolism and excretion in patients with acute
752 myeloid leukemia. *Cancer Chemother. Pharmacol.* **70**, 461–469 (2012).
753 62. Liu, D., Vader, G., Vromans, M. J. M., Lampson, M. A. & Lens, S. M. A. Sensing
754 chromosome bi-orientation by spatial separation of Aurora B kinase from kinetochore
755 substrates. *Science* **323**, 1350–1353 (2009).
756 63. Kallio, M. J., McCleland, M. L., Todd Stukenberg, P. & Gorbsky, G. J. Inhibition of
757 Aurora B kinase blocks chromosome segregation, overrides the spindle checkpoint,
758 and perturbs microtubule dynamics in mitosis. *Curr. Biol.* **12**, 900–905 (2002).
759 64. Wang, E., Ballister, E. R. & Lampson, M. A. Aurora B dynamics at centromeres create
760 a diffusion-based phosphorylation gradient. *J. Cell Biol.* **194**, 539–549 (2011).
761 65. Kim, Y., Holland, A. J., Lan, W. & Cleveland, D. W. Aurora kinases and protein
762 phosphatase 1 mediate chromosome congression through regulation of CENP-E. *Cell*
763 **142**, 444–455 (2010).
764 66. Cheeseman, I. M., Chappie, J. S., Wilson-Kubalek, E. M. & Desai, A. The Conserved
765 KMN Network Constitutes the Core Microtubule-Binding Site of the Kinetochore.
766 *Cell* **127**, 983–997 (2006).
767 67. Yao, X., Anderson, K. L. & Cleveland, D. W. The microtubule-dependent motor
768 centromere-associated protein E (CENP- E) is an integral component of kinetochore
769 corona fibers that link centromeres to spindle microtubules. *J. Cell Biol.* **139**, 435–447
770 (1997).
771 68. Qian, X. *et al.* Discovery of the first potent and selective inhibitor of centromere-
772 associated protein E: GSK923295. *ACS Med. Chem. Lett.* **1**, 30–34 (2010).
773 69. Griffis, E. R., Stuurman, N. & Vale, R. D. Spindly, a novel protein essential for
774 silencing the spindle assembly checkpoint, recruits dynein to the kinetochore. *J. Cell*
775 *Biol.* **177**, 1005–1015 (2007).
776 70. Ciferri, C. *et al.* Implications for Kinetochore-Microtubule Attachment from the
777 Structure of an Engineered Ndc80 Complex. *Cell* **133**, 427–439 (2008).
778 71. Trivedi, P. *et al.* The binding of Borealin to microtubules underlies a tension
779 independent kinetochore-microtubule error correction pathway. *Nat. Commun.* **10**,
780 (2019).
781 72. Wise, D. A. & Brinkley, B. R. Mitosis in cells with unreplicated genomes (MUGs):
782 Spindle assembly and behavior of centromere fragments. *Cell Motil. Cytoskeleton* **36**,
783 (1997).
784 73. Martin-Lluesma, S., Stucke, V. M. & Nigg, E. A. Role of Hec1 in spindle checkpoint
785 signaling and kinetochore recruitment of Mad1/Mad2. *Science* **297**, 2267–2270 (2002).
786 74. DeLuca, J. G., Moree, B., Hickey, J. M., Kilmartin, J. V. & Salmon, E. D. hNuf2
787 inhibition blocks stable kinetochore-microtubule attachment and induces mitotic cell
788 death in HeLa cells. *J. Cell Biol.* **159**, (2002).
789 75. Stumpff, J., von Dassow, G., Wagenbach, M., Asbury, C. & Wordeman, L. The
790 Kinesin-8 Motor Kif18A Suppresses Kinetochore Movements to Control Mitotic
791 Chromosome Alignment. *Dev. Cell* **14**, 252–262 (2008).
792 76. Mayr, M. I. *et al.* The Human Kinesin Kif18A Is a Motile Microtubule Depolymerase
793 Essential for Chromosome Congression. *Curr. Biol.* **17**, (2007).
794 77. Trupinić, M. *et al.* Twist of the mitotic spindle culminates at anaphase onset and
795 depends on microtubule-associated proteins along with external forces. *bioRxiv* (2020)
796 doi:10.1101/2020.12.27.424486.
797 78. Zeitlin, S. G., Shelby, R. D. & Sullivan, K. F. CENP-A is phosphorylated by Aurora B
798 kinase and plays an unexpected role in completion of cytokinesis. *J. Cell Biol.* **155**,
799 1147–1157 (2001).
800 79. Chandrasekaran, A., Upadhyaya, A. & Papoian, G. A. Remarkable structural

transformations of actin bundles are driven by their initial polarity, motor activity, crosslinking, and filament treadmilling. *PLoS Comput. Biol.* **15**, (2019).
80. Weirich, K. L. *et al.* Liquid behavior of cross-linked actin bundles. *Proc. Natl. Acad. Sci. U. S. A.* **114**, 2131–2136 (2017).
81. Yoshida, S. *et al.* Prc1-rich kinetochores are required for error-free acentrosomal spindle bipolarization during meiosis I in mouse oocytes. *Nat. Commun.* **11**, (2020).
82. Maton, G. *et al.* Kinetochore components are required for central spindle assembly. *Nat. Cell Biol.* **17**, 697–705 (2015).
83. Liu, X. *et al.* Mitotic motor CENP-E cooperates with PRC1 in temporal control of central spindle assembly. *J. Mol. Cell Biol.* **12**, 654–665 (2020).
84. Vitre, B. *et al.* Kinetochore-microtubule attachment throughout mitosis potentiated by the elongated stalk of the kinetochore kinesin CENP-E. *Mol. Biol. Cell* **25**, 2272–2281 (2014).
85. Kim, Y., Heuser, J. E., Waterman, C. M. & Cleveland, D. W. CENP-E combines a slow, processive motor and a flexible coiled coil to produce an essential motile kinetochore tether. *J. Cell Biol.* **181**, 411–419 (2008).
86. Wei, R. R., Sorger, P. K. & Harrison, S. C. Molecular organization of the Ndc80 complex, an essential kinetochore component. *Proc. Natl. Acad. Sci. U. S. A.* **102**, 5363–5367 (2005).
87. Vallee, R. B., Wall, J. S., Paschal, B. M. & Shpetner, H. S. Microtubule-associated protein 1c from brain is a two-headed cytosolic dynein. *Nature* **332**, 561–563 (1988).
88. Shrestha, R. L. & Draviam, V. M. Lateral to end-on conversion of chromosome-microtubule attachment requires kinesins cenp-e and MCAK. *Curr. Biol.* **23**, 1514–1526 (2013).
89. Winey, M. *et al.* Three-dimensional ultrastructural analysis of the Saccharomyces cerevisiae mitotic spindle. *J. Cell Biol.* **129**, 1601–1615 (1995).
90. Landry, J. J. M. *et al.* The genomic and transcriptomic landscape of a hela cell line. *G3 Genes, Genomes, Genet.* **3**, 1213–1224 (2013).
91. Murata-Hori, M. & Wang, Y. L. The kinase activity of aurora B is required for kinetochore-microtubule interactions during mitosis. *Curr. Biol.* **12**, (2002).
92. Yang, J. *et al.* AZD1152, a novel and selective aurora B kinase inhibitor, induces growth arrest, apoptosis, and sensitization for tubulin depolymerizing agent or topoisomerase II inhibitor in human acute leukemia cells in vitro and in vivo. *Blood* **110**, (2007).
93. Wood, K. W. *et al.* Antitumor activity of an allosteric inhibitor of centromere-associated protein-E. *Proc. Natl. Acad. Sci. U. S. A.* **107**, 5839–5844 (2010).
94. Bennett, A. *et al.* Cenp-E inhibitor GSK923295: Novel synthetic route and use as a tool to generate aneuploidy. *Oncotarget* **6**, 20921–20932 (2015).
95. Rizk, A. *et al.* Segmentation and quantification of subcellular structures in fluorescence microscopy images using Squassh. *Nat. Protoc.* **9**, 586–596 (2014).

843 **METHODS**

844

845 **Cell lines and culture**

846 Experiments were carried out using unlabeled human HeLa-TDS cells (also referred to as
847 untransfected HeLa cells) from the High-Throughput Technology Development Studio (Max
848 Planck Institute of Molecular Cell Biology and Genetics, Dresden, Germany), HeLa-Kyoto
849 BAC lines stably expressing PRC1-GFP (also referred to as HeLa PRC1-GFP cells) are
850 courtesy of Ina Poser and Tony Hyman (Max Planck Institute of Molecular Cell Biology and
851 Genetics, Dresden, Germany), and human hTERT-RPE1 (hTERT-immortalized retinal
852 pigment epithelium) cells stably expressing CENP-A-GFP and Centrin1-GFP, courtesy of
853 Alexey Khodjakov (Wadsworth Center, New York State Department of Health, Albany, NY,
854 USA). All cell lines were cultured in flasks in Dulbecco's Modified Eagle's Medium with 1 g/L
855 D-glucose, pyruvate and L-glutamine (DMEM, Lonza, Basel, Switzerland), supplemented with
856 10% (vol/vol) heat-inactivated Fetal Bovine Serum (FBS, Sigma Aldrich, St. Louis, MO, USA)
857 and penicillin (100 IU/mL)/streptomycin (100 mg/mL) solution (Lonza, Basel, Switzerland).
858 For the selection of HeLa PRC1-GFP cell lines, 50 µg/ml geneticin was added to the medium
859 (Life Technologies, Waltham, MA, USA). The cells were kept at 37°C and 5% CO_2 in a
860 humidified incubator (Galaxy 170S CO_2, Eppendorf, Hamburg, Germany) and regularly
861 passaged at the confluence of 70-80%.

862

863 **Sample preparation, siRNA, plasmids, and dyes**

864 At 80% confluence, DMEM medium was removed from the flask and cells were washed with
865 5 ml of phosphate buffered saline (PBS). Then, 1 ml 1% trypsin/ethylenediaminetetraacetic
866 acid (EDTA, Biochrom AG, Berlin, Germany) was added to the flask and cells were incubated
867 at 37°C and 5% CO_2 in a humidified incubator for 5 minutes. After the incubation, trypsin was
868 blocked by adding 2 ml of DMEM medium. For RNAi experiments, the cells were seeded to
869 reach 60% confluence the next day and cultured on 35 mm uncoated dishes with 0.17 mm (#1.5
870 coverglass) glass thickness (MatTek Corporation, Ashland, MA, USA) in 2 mL DMEM
871 medium with the supplements described above. After one day of growth, cells were transfected
872 with either targeting or non-targeting siRNA constructs which were diluted in OPTI-MEM
873 medium (Life Technologies, Waltham, MA, USA) to a final concentration of 100 nM in the
874 medium with cells. All transfections were performed 48 hours prior to imaging using
875 Lipofectamine RNAiMAX Reagent (Life Technologies, Waltham, MA, USA) according to the
876 instructions provided by the manufacturer. After four hours of treatment, the medium was

877 changed to the DMEM medium. The constructs used were human HAUS6 siRNA (L-018372-
878 01-0005, Dharmacon, Lafayette, CO, USA), human ON-TARGET plus SMART pool CENP-
879 E siRNA (L-003252-00-0010, Dharmacon, Lafayette, CO, USA), ON-TARGET human
880 CCDC99 siRNA (L-016970-00-0010, Dharmacon, Lafayette, CO, USA), human Ndc80
881 siRNA (HA12977117-004; Merck, Darmstadt, Germany), human ON-TARGET PRC1 siRNA
882 (L-019491-00-0020, Dharmacon) and control siRNA (D-001810-10-05, Dharmacon,
883 Lafayette, CO, USA).
884 For experiments with CENP-B-INCENP-GFP, unlabeled HeLa-TDS cells were
885 transfected with CENP-B-INCENP-GFP (Addgene, plasmid #45238), and for live-cell
886 imaging also with mCherry-PRC1 plasmid provided by Casper C. Hoogenraad (Utrecht
887 University, Utrecht, The Netherlands). 1×10^6 cells were transfected using Lipofectamine 3000
888 Reagent (L3000001, Life Technologies, Waltham, MA, US) with 1.5 µg of plasmid DNA for
889 both plasmids. For CENP-E overexpression experiments, unlabeled HeLa-TDS cells were
890 transfected with 2 µg of CENP-E-GFP plasmid (gift from Marin Barišić, Danish Cancer
891 Society Research Center, Copenhagen, Denmark). To overexpress PRC1, unlabeled HeLa-
892 TDS cells were transfected with 5 µg of mCherry-PRC1 plasmid. Transfection of both
893 unlabeled HeLa-TDS and HeLa PRC1-GFP cells was performed 25–35 h before imaging.
894 In order to visualize microtubules, human hTERT-RPE1 cells stably expressing CENP-
895 A-GFP and Centrin1-GFP and unlabeled HeLa-TDS cells were stained to a final concentration
896 of 100 nM with a far-red silicon rhodamine (SiR)-tubulin-670 dye (Spirochrome, Stein am
897 Rhein, Switzerland), 45 minutes to 2 hours prior to imaging. In order to avoid dye efflux, a
898 broad-spectrum efflux pump inhibitor verapamil (Spirochrome, Stein am Rhein, Switzerland)
899 was added at a final concentration of 0.5 µM to the cells along with SiR-tubulin. For
900 chromosome visualization, HeLa PRC1-GFP cells were stained with 100 nM SiR-DNA dye
901 for 20 minutes to 2 hours prior to imaging. To identify the cells in mitosis by condensed
902 chromosomes in the PRC1 overexpression experiment on unlabeled HeLa-TDS cells, 50 µL of
903 NucBlue Live Ready Probes Reagent (Hoechst 33342, Invitrogen by Thermo Fisher Scientific,
904 Waltham, MA, USA) was added to the dishes 1 min before imaging.
905
906 **Drug treatments**
907 The stock solution of the Aurora B kinase inhibitor Barasertib (AZD1152-HQPA,
908 Selleckchem, Munich, Germany) was prepared in Dimethyl sulfoxide (DMSO) to a final
909 concentration of 1 mM. The working solution was prepared in DMEM at 600 nM and at the
910 time of treatment, the working solution was added to cells at 1:1 volume ratio to obtain a final

911 concentration of 300 nM; IC50 is 0.35 nM for this compound[92]. Barasertib was added at early
912 prometaphase rosette in HeLa PRC1-GFP cell line. Appearance of predominantly
913 prometaphase-like spindles[63] in the sample imaged 1 hour post-treatment confirmed the effect
914 of Barasertib on Aurora B.

915 The stock solution of the CENP-E inhibitor GSK-923295 (MedChemExpress,
916 Monmouth Junction, NJ, USA) was prepared in DMSO at a final concentration of 8 mM. The
917 working solution was prepared in DMEM at 200 nM. At the time of treatment, the working
918 solution was added to cells at 1:1 volume ratio to obtain a final concentration of 100 nM; IC50
919 value of compound is 3.2 nM[93]. GSK-923295 was added at early prometaphase rosette in HeLa
920 PRC1-GFP cell line immediately before the start of imaging, and 2 hours before imaging in
921 hTERT-RPE1 cell line expressing CenpA-GFP and Centrin1-GFP. Appearance of spindles
922 blocked in prometaphase with a fraction of kinetochores trapped around polar region of the
923 spindle at 30 minutes post-treatment[94] confirmed the effect of GSK-923295. For hTERT-RPE1
924 cells, mock treatment was the same concentration of DMSO that was used for preparation of
925 the inhibitors.

926 Nocodazole (HY-13520, MedChemExpress, Monmouth Junction, NJ, USA) working
927 solution was prepared in DMEM at 2 μM. At the time of treatment, the working solution was
928 added to cells at 1:1 volume ratio to obtain a final concentration of 1 μM. Nocodazole was
929 added at early prometaphase rosette in HeLa PRC1-GFP cell line immediately before the start
930 of imaging.

931 Monastrol (HY-101071A/CS-6183, MedChemExpress, Monmouth Junction, NJ, USA)
932 working solution (100 μM) was added in the dish with untransfected HeLa cells at a final
933 concentration of 100 nM.

934

935 **Inducing mitosis with unreplicated genome (MUG)**

936 MUG is induced by incubation of cells in hydroxyurea and caffeine[72], a gift from Anđela
937 Horvat and Neda Slade (Laboratory for protein dynamics, Ruđer Bošković Institute, Zagreb,
938 Croatia). The stock solutions of hydroxyurea and caffeine were prepared at a concentration of
939 175 mM and 200 mM, respectively. The stock solution was diluted in DMEM to the final
940 concentration of 2 mM for hydroxyurea and 5 mM for caffeine. The amount of $1x10^5$ HeLa
941 PRC1-GFP cells were counted using the Improved Neubauer chamber (BRAND GMBH + CO
942 KG, Wertheim, Germany), seeded and cultured in 2 ml DMEM at 37°C and 5% CO_2 on 35 mm
943 glass coverslip uncoated dishes with 0.17 mm (#1.5 coverglass) glass thickness (MatTek
944 Corporation, Ashland, MA, USA). After 12 hours, the medium was replaced with 2 mL DMEM

containing 2 mM hydroxyurea and incubated for 20 hours at 37°C and 5% CO_2. After 20 hours, the medium was again replaced with a medium containing 2 mM hydroxyurea and 5 mM caffeine and the cells were again incubated at 37°C and 5% CO_2. The cells were imaged 18 hours later.

Immunocytochemistry

HeLa cells expressing PRC1-GFP and untransfected HeLa cells were grown on glass-bottom dishes (14 mm, No. 1.5, MatTek Corporation, Darmstadt, Germany) and fixed by 1 ml of ice-cold methanol for 1 min at -20°C. Following fixation, cells were washed 3 times for 5 minutes with 1 ml of PBS and permeabilized with 0.5% Triton-X-100 in water for 15 minutes at room temperature. To block unspecific binding, cells were incubated in 1 ml of blocking buffer (1% normal goat serum, NGS) for 1 hour at room temperature. Cells were then washed 3 times for 5 minutes with 1 ml of PBS and incubated with 500 µl of primary antibody solution overnight at 4°C. The following primary antibodies were used: mouse monoclonal PRC1 (sc-376983, Santa Cruz Biotechnology), diluted 1:100, rat anti-alpha-tubulin YL1/2 (MA1-80017, Invitrogen, CA, SAD), diluted 1:500, mouse IgG monoclonal anti-GFP (Ref 11814460001, LOT42903200, Roche), diluted 1:100, rabbit anti-alpha-tubulin (SAB4500087, LOT 310379, Sigma Aldrich), diluted 1:500, human anti-CREST (15-235, Antibodic sinc), 1:100, Rabbit anti-CENP-E (C7488, Sigma Aldrich), diluted 1:100, Rabbit anti-Aurora B (ab239837, Abcam), diluted 1:100, anti-Hec1 (ab3613, Abcam), diluted 1:100, anti-Spindly (A301-354A, Biomolecules), diluted 1:100, anti-phospho-CENP-A (Ser7) (07-232, Sigma-Aldrich), diluted 1:500. After primary antibody, cells were washed in PBS and then incubated in 500 µL of secondary antibody solution for 45 min at room temperature. The following secondary antibodies were used: donkey anti-mouse IgG Alexa Fluor 594, diluted 1:250 (ab150112, Abcam, Cambridge, UK), donkey anti-rabbit IgG Alexa Fluor 647 (ab150075, Abcam) and donkey anti-rat IgG Alexa Fluor 647 (ab150155, Abcam), Goat anti-human IgG 594 (ab96909, Abcam), all diluted 1:500. Finally, cells were washed with 1 mL of PBS, 3 times for 10 min. This fixation was used for imaging HeLa PRC1-GFP cell line for siRNA silencing control, kinetochore and PRC1 visualization in vertical rosettes and for PRC1 visualization in different treatments (CENP-E overexpression, Aurora B relocalization) in untransfected HeLa cells.

To visualize alpha-tubulin in STED resolution in HeLa PRC1-GFP cell line, ice-cold methanol protocol was avoided because it destroyed the unstable fraction of microtubules. Cells were washed with cell extraction buffer (CEB) and fixed by a microtubule-preserving mixture of 3.2% paraformaldehyde (PFA) and 0.25% glutaraldehyde (GA) in microtubule-

979 stabilizing PEM buffer (0.1 M PIPES, 0.001 M MgCl2 x 6 H2O, 0.001 M EDTA, 0.5 % Triton-
980 X-100) for 10 min at room temperature (Heuser and Kirschner, 1980). After fixation with PFA
981 and GA, for quenching, cells were incubated in 1 mL of freshly prepared 0.1% borohydride in
982 PBS for 7 min and after that in 1 mL of 100 mM NH_4Cl and 100 mM glycine in PBS for 10
983 min at room temperature. To block unspecific binding of antibodies, cells were incubated in
984 500 µL blocking/permeabilization buffer (1% normal goat serum and 0.5% Triton-X-100 in
985 water) for 2 hours at room temperature. Cells were then incubated in 500 µL of primary
986 antibody solution overnight at 4°C. After the incubation with a primary antibody, cells were
987 washed 3 times for 10 minutes with 1 ml of PBS and then incubated with 500 µl of secondary
988 antibody for 2 hours at room temperature. This protocol was used in all experiments where
989 tubulin is visualized in STED mode. In all fixations, DAPI (1 µg/mL) was used for
990 chromosome visualization.
991
992 **Imaging**
993 *STED microscope system (Abberior Instruments)*. STED microscopy was performed using the
994 Expert Line easy3D STED microscope system (Abberior Instruments) with a 60x/1.2
995 UPLSAPO 60XW water objective (Olympus), avalanche photodiode (APD) detector, and
996 Imspector software to acquire spindle cross-sections in horizontally and vertically oriented
997 spindles in different stages of mitosis of HeLa cells expressing PRC1-GFP, immunostained for
998 tubulin, with DNA stained by DAPI. STED images of tubulin were acquired in a single plane
999 in the Alexa 594 channel with the excitation and depletion laser power at 35%, and pixel size
1000 set 20 nm. PRC1 and DNA were imaged in the same spindles in the confocal mode. Confocal
1001 mode was also used to image fixed prometaphase rosettes and metaphase spindles in
1002 untransfected and PRC1-GFP HeLa cells using eGFP and DAPI excitation lasers to visualize
1003 GFP and DAPI, respectively, or Alexa 488, 594, 647 excitation lasers depending on the
1004 secondary antibody. The laser power was 10%, except for Alexa 647 where it was 5%. Pixel
1005 size was 50 nm for prometaphase spindles and for imaging bridging fibers in metaphase, and
1006 100 nm for metaphase spindles. Z-stacks of 41 focal planes, except in experiments on lagging
1007 kinetochores where the number of planes was 20, were acquired with 0.5 µm spacing to cover
1008 the whole spindle. For live cell imaging of vertical metaphase spindles in HeLa PRC1-GFP
1009 cell line, the middle plane was recognized as the plane in which the bundles appear as clear
1010 dots of PRC1-GFP and the spindle cross-section is filled with chromosomes. Four planes close
1011 to the spindle midplane were acquired, separated by 0.5 µm. Pixel size was 50 nm. Laser power
1012 for eGFP excitation laser was 15%, and for SiR-DNA was 5%. Live cell imaging of horizontal

1013 metaphase spindles was performed in HeLa PRC1-GFP cell line with Z-stacks of 41 planes
1014 using eGFP excitation light at 10% laser power and 5% laser power for SiR-DNA channel.
1015 Pixel size was 100 nm. The bundling assay was applied for imaging of tubulin with SiR-tubulin
1016 dye in HeLa PRC1-GFP cell line. Time-lapse images of the spindle midplane were acquired
1017 using only SiR excitation laser with 8% power. Time between repetitions was 1 minute and
1018 pixel size was 100 nm.

1019 *Dragonfly spinning disk confocal microscope system (Andor Technology).* To image
1020 the formation of PRC1-labeled bundles in HeLa cells expressing PRC1-GFP (bundling assay),
1021 confocal live-cell imaging was performed on a Dragonfly spinning disk microscope (Andor
1022 Technology, Belfast) using 63x/1.47 HC PL APO glycerol objective (Leica, Belfast) and Zyla
1023 4.2P scientific complementary metal oxide semiconductor (sCMOS) camera (Andor
1024 Technology). Images were acquired using Fusion software. During imaging, cells were
1025 maintained at 37ºC and 5% CO_2 within a heating chamber (Okolab, Pozzuoli, NA, Italy). Only
1026 cells with vertically oriented spindles were imaged as follows: first a 41 plane Z-stack was
1027 acquired to cover the whole spindle using both 478 nm and 640 nm excitation light at a 10%
1028 and 5% laser power, respectively. Then a time-series of images was required using only 478
1029 nm excitation light. Every repetition recorded 9 middle frames of the vertical spindle, forming
1030 a stack of 9 slices separated 0.5 µm. Time between repetitions was 5.4 seconds. After the time-
1031 series, the second Z-stack was acquired, again using both excitation lasers. Total time-lapse
1032 movie was 9 minutes long. The same protocol was used for experiments with untreated cells,
1033 Haus6-depleted cells, and cells treated with Barasertib, GSK-923295, and nocodazole. For
1034 Ndc80, Haus6, and Spindly silencing control, a 41 plane Z-stack was acquired to cover the
1035 whole spindle using 478 nm, 620 nm and 408 nm excitation light at a 10% for first two and 5%
1036 laser power for DAPI channel. For all images pixel size was 100 nm.

1037 *Opterra confocal microscope system (Bruker).* For counting the number of bundles and
1038 for bundle trajectories, HeLa cells expressing PRC1-GFP and hTERT-RPE1 cells expressing
1039 CENP-A-GFP and Centrin1-GFP were imaged using Bruker Opterra Multipoint Scanning
1040 Confocal Microscope (Bruker Nano Surfaces, Middleton, WI, USA). The system was mounted
1041 on a Nikon Ti-E inverted microscope equipped with a Nikon CFI Plan Apo VC 100x/1.4
1042 numerical aperture oil objective (Nikon, Tokyo, Japan). The system was controlled with the
1043 Prairie View Imaging Software (Bruker). During imaging, cells were maintained at 37°C in
1044 Okolab Cage Incubator (Okolab, Pozzuoli, NA, Italy). For optimal resolution and signal-to-
1045 noise ratio, 22 nm slit was used. For excitation of GFP, 488 nm diode laser line was used. The
1046 excitation light was separated from the emitted fluorescence by using Opterra Dichroic and

1047 Barrier Filter Set 405/488/561/640. Images were captured with an Evolve 512 Delta Electron
1048 Multiplying Charge Coupled Device (EMCCD) Camera (Photometrics, Tucson, AZ, USA)
1049 using 150-200 ms exposure times. For counting the number of bundles, Z-stacks of 41 focal
1050 planes were acquired with 0.5 µm spacing to cover the whole spindle. Horizontally oriented
1051 prometaphase spindles of HeLa PRC1-GFP cells with added SiR-DNA dye and hTERT-RPE1
1052 cells expressing CENP-A-GFP and Centrin1-GFP with added SiR-tubulin dye were filmed
1053 every 10 and 5 minutes, respectively. Prometaphase cells were recognized by non-congressed
1054 chromosomes and relatively small spindle size. To image the dynamics of PRC1-labeled
1055 bundles in HeLa cells expressing PRC1-GFP, confocal live-cell imaging was performed. Only
1056 cells with vertically oriented spindles were imaged as follows: first a 41 plane Z-stack was
1057 acquired to cover the whole spindle using both 488 nm and 640 nm excitation light. Then a
1058 time-series of images was required using only 488 nm excitation light. Every repetition
1059 recorded 9 middle frames of the vertically oriented spindle, forming a stack of 9 slices separated
1060 0.5 µm. Time between repetitions was 2.7 seconds. After the time-series, a second Z-stack was
1061 acquired, again using both excitation lasers. Total time lapse movie was 4.5 minutes long. Laser
1062 powers were 10% and 5% for 488 nm and 640 nm excitation light, respectively.
1063
1064 **Image processing and data analysis**
1065 All images were analyzed in Fiji/ImageJ (National Institutes of Health, Bethesda, MD, USA).
1066 Raw images were used for quantification. Contrast was adjusted for clarity of presentation in
1067 the figures. MatLab (MathWorks, Natick, MA, USA) was used to create the plots, Rstudio (R
1068 Foundation for Statistical Computing, Vienna, Austria) to transform the horizontally oriented
1069 spindles into an end-on view. Figures were assembled in Adobe Illustrator CS5 (Adobe
1070 Systems, Mountain View, CA, USA).
1071 *Bundling assay.* For analysis of bundle formation, Squash plugin in Fiji was used in the
1072 PRC1-GFP channel of the middle plane of the spindle. Segmentation was performed using
1073 Squash [95]. In the main graphical user interface Squash window, we set the parameter for
1074 background subtraction option, entering the window edge lengths in units of 14 pixels. Object
1075 detection was performed over the entire image. The higher value of the regularization
1076 parameter of 0.1 was used to avoid the segmenting noise-induced small intensity peaks.
1077 Intensity values were normalized between 0 for the smallest value occurring in the image, and
1078 1 for the largest value. The sub-pixel segmentation was selected. The resolution of the
1079 segmentation was increased by an oversampling factor of 8 for 2D images. Local intensity
1080 estimation parameter was set to automatic. The Poisson model, recommended for confocal

1081 microscopes, was chosen. The following visualization options were selected: object intensities,
1082 number of objects and the mean object size in terms of area. Validation was performed by
1083 manually measuring object segmentation in the middle plane of a representative spindle.

1084 *Number of bundles.* To count the bundles, horizontally oriented spindles were
1085 transformed into vertical (end-on) orientation using the code written in R programming
1086 language in R Studio (R Core Team., 2016). Before the transformation, the Z-stack of the
1087 spindle in a single channel was rotated in Fiji so that the spindle major axis was approximately
1088 parallel to the x-axis. The aberrations caused by refractive index mismatch between immersion
1089 oil and aqueous sample were taken into account in the program by multiplying Z-step size by
1090 a correction factor of 0.81 to obtain the correct Z-distance. This factor corresponds to the ratio
1091 of the cell diameter in y and z direction, assuming that a mitotic cell is spherical. Bundles were
1092 counted on the sum intensity images of 5 central planes of the transformed spindle. The number
1093 of bundles was determined by counting the bright spots using Multi point tool in ImageJ.

1094 *Protein silencing.* Analysis of the immunofluorescence signal was performed on the
1095 sum of all 41 planes. The territory of the spindle was encircled with a segmented line in Fiji
1096 and sum intensity was measured.

1097 *PRC1 intensity of early formed bundles in the prometaphase rosette.* To measure the
1098 bundle intensity in vertically oriented early prometaphase rosette, bundles were encircled in
1099 Fiji and sum intensity was measured in only one plane of the cross section where the bundle
1100 was of highest intensity. Bundles with bound kinetochores were measured in the plane where
1101 the kinetochore was visible close to the bundle. The brightest bundles (usually two) that
1102 connect the spindle poles in a straight line were not measured because they are formed before
1103 nuclear envelope breakdown. Thus, only bundles in the prometaphase network were measured.

1104 *PRC1 intensity of bundles in metaphase.* To measure the bundle intensity in vertically
1105 oriented metaphase spindles, each bundle was encircled in Fiji with a fixed-size circle (p=0.61
1106 μm^2) and mean intensity was measured in only one plane of the cross-section where DNA
1107 covered the whole cross-section. To calculate the PRC1 intensity of the bundle, mean intensity
1108 of PRC1 in the cytoplasm was subtracted from bundle PRC1 intensity. Furthermore, to correct
1109 for the differences in PRC1 expression in different cells, the PRC1 bundle intensity was divided
1110 by the mean intensity of PRC1 in the cytoplasm to get the normalized PRC1 intensity.

1111 *PRC1 intensity of the network in early prometaphase.* To measure the network intensity
1112 in vertically oriented prometaphase spindles, the region excluding the brightest bundles (the
1113 ones formed before nuclear envelope breakdown) was encircled in Fiji and mean intensity was
1114 measured in only one plane. As for the PRC1 intensity of bundles, the mean intensity of PRC1

1115 in the cytoplasm was subtracted from the network PRC1 intensity, and the result was divided
1116 by the mean intensity of PRC1 in the cytoplasm to get the normalized PRC1 intensity.
1117 *Tubulin intensity of bridging fibers in metaphase.* Intensity of bridging fibers was
1118 measured on metaphase spindles. A line was drawn along the bridging fiber using Line tool in
1119 Fiji, only the region beneath the kinetochore pair was measured. Intensity of tubulin was
1120 measured at the midpoint of the line intensity plot. Furthermore, to correct for the differences
1121 in tubulin signal in different cells, tubulin bundle intensity was divided by the mean intensity
1122 of tubulin in the cytoplasm to get the normalized tubulin intensity.
1123 *PRC1 line intensity in metaphase.* In HeLa PRC1-GFP cell line, a line was drawn from
1124 pole to pole in a metaphase spindle, which was recognized by fully aligned chromosomes in
1125 control cells. In treatments that cause impaired chromosome congression, spindles with most
1126 chromosomes aligned were chosen. Line intensity plot was made by subtracting the
1127 cytoplasmatic PRC1 signal and dividing by it, providing the normalized PRC1 intensity.
1128 *Aurora B-PRC1 correlation.* Individual PRC1-labeled bridging fibers were encircled
1129 with a circle that goes from the top edge of the bundle to the bottom edge, and the sum intensity
1130 was measured. The same-size circle was used to measure the sum intensity of the Aurora B
1131 signal on the associated centromere. Normalized intensity of PRC1 and Aurora B was obtained
1132 by subtracting the cytoplasmatic mean intensity of the respective protein and dividing by it.
1133 *Phosphorylation of outer kinetochore.* Sum intensity of CREST and CENP-A signal
1134 was measured in prometaphase cells. The spindle was boxed in a fixed square that was same
1135 for all cells. The intensity ratio was expressed by dividing the CENP-A-Ser7P sum intensity
1136 by the CREST sum intensity.
1137 *Spindle parameters.* Spindle width and length were measured on horizontally oriented
1138 metaphase spindles using Line tool in Fiji.
1139 *Manual bundle tracking.* The 2D trajectories of the bundles and their coordinates were
1140 tracked using Manual tracking tool to obtain bundle trajectories. The movement of all bundles
1141 was represented with respect to the brightest bundle(s) that appear before nuclear envelope
1142 breakdown and do not have chromosomes attached in early prometaphase, using Manual drift
1143 correction plugin in Fiji.
1144 *DNA occupancy in the metaphase.* Sum intensity of SiR-DNA signal from 41 planes
1145 was used for measurement of DNA occupancy in the equatorial region of the spindle.
1146 Proportion of DNA at the metaphase plate over time was measured as mean intensity of the
1147 DNA within the line covering the equatorial region divided by the intensity of all DNA in the
1148 cell. The line covering the equatorial region was defined in metaphase so that its width was

1149 equal to the width of the metaphase plate and length equal to spindle width. The same line was
1150 used for all time frames.

1151 *Lagging kinetochores* were identified by the CREST signal together with the DNA
1152 signal in the central part of the spindle in anaphase, between the two segregated groups of
1153 kinetochores/chromosomes.

1154 *Statistical analysis and figure preparation.* Graphs were generated in Matlab
1155 (MathWorks, Natick, MA, USA). Fiji was used to scale images and adjust brightness and
1156 contrast. Figures were assembled in Illustrator (Adobe Systems, Mountain View, CA, USA).
1157 Data are given as mean ± s.e.m., unless otherwise stated. Means of two groups were compared
1158 by Student's t-test (two-tailed and two-sample unequal-variance), and means of more than two
1159 groups by one-way ANOVA test and Tukey's HSD post hoc test, $p < 0.05$ was considered
1160 statistically significant. The numbers of microtubule bundles, cells, and independent
1161 experiments are given in the figure panels.
1162

Theoretical model

To describe the dynamical transition from array like distribution of microtubules to well organized multiple bundles during prometaphase, we consider both equilibrium and non equilibrium processes involving microtubules, crosslinking proteins, chromosomes, and kinetochores. The model we construct is placed in an one dimensional geometry with spatial coordinate x, taken from the part of the circumference of the disc that is obtained by taking a vertical cross section at the mid plane of a prometaphase spindle as shown in Fig 5A. Microtubules and crosslinkers are described as point like objects with densities $\tilde{\rho}$ and $\tilde{\psi}$, respectively. For simplicity, we assume that crosslinker have a uniform density.

In our model, we include interactions between microtubules, crosslinkers and kinetochores. We describe these interactions by constructing a Landau–Ginzburg free energy:

$$F[\tilde{\rho}] = \int d\tilde{x}\Big\{\frac{\tilde{w}}{4}\tilde{\rho}^4 + \frac{\tilde{\kappa}}{2}\Big(\frac{\partial\tilde{\rho}}{\partial\tilde{x}}\Big)^2 - \tilde{\zeta}\tilde{\rho}\tilde{\psi}\tilde{\rho} - \tilde{\alpha}\tilde{\rho}^2\delta(\tilde{x} \pm (2n+1)\tilde{d})\Big\}. \tag{1}$$

In the first term we describe local microtubule repulsion as nonlinear interaction with strength $\tilde{w}$. The second term captures a non-local repulsion of strength $\tilde{\kappa}$, which is coming from interaction between chromosomes and microtubules. The third term describes an attractive interaction between two microtubules mediated by crosslinkers and with coupling constant $\tilde{\zeta}$. The last term represents attraction between kinetorchores and microtubules of strength $\tilde{\alpha}$. This local attraction is described by Dirac delta function. In our system, kinetochores are placed in regular intervals of given integer index n, forming lattice-like structure with spacing $2\tilde{d}$.

Time evolution of microtubule density can be obtained by writing a conserved dynamics of $\tilde{\rho}$ by minimizing $F[\tilde{\rho}]$ and incorporating non equilibrium process of appearance and disappearance of microtubules in our region of interest. Rapid polymerization and depolymerization of microtubule filaments causes the processes of creation and annihilation of those filaments in the mid plane of the vertically oriented spindle. We assume that microtubules are created with a constant rate ω_{on} and get disassembled with a rate ω_{off}. Finally, we calculate how microtubule density changes in time t as

$$\frac{\partial\tilde{\rho}}{\partial t} = \tilde{w}\tilde{M}_\rho\frac{\partial^2\tilde{\rho}^3}{\partial\tilde{x}^2} - \tilde{\kappa}\tilde{M}_\rho\frac{\partial^4\tilde{\rho}}{\partial\tilde{x}^4} - 2\tilde{\zeta}\tilde{M}_\rho\tilde{\psi}\tilde{M}_\rho\frac{\partial^2\tilde{\rho}}{\partial\tilde{x}^2} - 2\tilde{\alpha}\tilde{M}_\rho\frac{\partial^2}{\partial\tilde{x}^2}\{\tilde{\rho}\delta(\tilde{x} \pm (2n+1)\tilde{d})\} + \omega_{on}\tilde{\rho}_b - \omega_{off}\tilde{\rho}$$

Here, $\tilde{\rho}_b$ denotes microtubule nucleation density in the cytoplasm and $\tilde{M}_\rho$ is microtubule mobility. Now, we proceed to make this time evolution equation dimensionless by using a length scale $x = \tilde{x}(\tilde{w})^{-\frac{1}{3}}$ and a time scale $\tau = t\omega_{off}$ and obtain,

$$\frac{\partial\rho}{\partial\tau} = M_\rho\frac{\partial^2\rho^3}{\partial x^2} - \kappa M_\rho\frac{\partial^4\rho}{\partial x^4} - 2\zeta M_\rho\psi\frac{\partial^2\rho}{\partial x^2} - 2\bar{\alpha}M_\rho\frac{\partial^2}{\partial x^2}\{\rho\delta(x \pm (2n+1)d)\} + \omega\rho_b - \rho, \tag{2}$$

where $\rho = \tilde{\rho}\tilde{w}^{\frac{1}{3}}$, $\psi = \tilde{\psi}\tilde{w}^{\frac{1}{3}}$, $\zeta = \tilde{\zeta}\tilde{w}^{-\frac{2}{3}}$, $\kappa = \tilde{\kappa}\tilde{w}^{-1}$, $\bar{\alpha} = \tilde{\alpha}\tilde{w}^{-1}$, $d = \tilde{d}\tilde{w}^{-\frac{1}{3}}$, $\rho_b = \tilde{\rho}_b\tilde{w}^{\frac{1}{3}}$, $M_\rho = \tilde{M}_\rho\omega_{off}^{-1}$ and $\omega = \frac{\omega_{on}}{\omega_{off}}$.

A. Boundary conditions and steady state density profiles

To study the kinetochore driven bundling of microtubules in the linear regime, we construct linearized steady state equation with steady state microtubule density ρ_f from Eq.(2) by setting $\rho = \rho_s + \rho_f$, where $\rho_s = \frac{\omega_{on}}{\omega_{off}}\rho_b$. The steady state equation with delta-function at $\pm d$ reads as

$$M_\rho\Big[(3\rho_s^2 - 2\zeta\psi)\frac{\partial^2\rho_f}{\partial x^2} - \kappa\frac{\partial^4\rho_f}{\partial x^4}\Big] - \rho_f - 2\bar{\alpha}M_\rho\frac{\partial^2}{\partial x^2}\{(\rho_s + \rho_f)\delta(x \pm d)\} = 0 \tag{3}$$

The last term in Eq.(3) is vanishing at all positions except at $\pm d$. Thus, we first solve Eq.(3) between boundary points by searching for solutions in the form $\rho_f(x) = \sum_{j=1}^{4} C_j e^{-im_j x}$ and obtain

$$m^4 + \eta_1 m^2 + \eta_2 = 0, \tag{4}$$

where, $\eta_1 = \frac{3\rho_s^2 - 2\zeta\psi}{2\kappa}$ and $\eta_2 = \frac{1}{\kappa M_\rho}$. Symmetry of Eq.(4) ensures the four solution $m_{1,2,3,4}$ can be written as $m_3 = -m_1$ and $m_4 = -m_2$ and consequently we obtain the density profile in steady state as

$$\rho_f(x) = C_1 e^{-im_1 x} + C_2 e^{-im_2 x} + C_3 e^{im_1 x} + C_4 e^{im_2 x}, \tag{5}$$

$C_{1,..,4}$ being constants of integration. The structure of the system with two attractive δ functions at $\pm d$ ensures the existence of mirror symmetry $\rho_f(-x) = \rho_f(x)$ and Eq.(5) reduces to,

$$\rho_f(x) = C_1(e^{im_1 x} + e^{-im_1 x}) + C_2(e^{im_2 x} + e^{-im_2 x}) \tag{6}$$

Performing repeated integration of Eq.(3) and finally in the $\lim_{\epsilon \to 0}$, $\int_{d-\epsilon}^{d+\epsilon}$ around the δ function yields,

$$\kappa[\rho_f'(-d) - \rho_f'(d)] + 2\bar{\alpha}\rho_s + 2\bar{\alpha}\rho_f(d) = 0 \tag{7}$$

Here, we have used the translational invarience of the density $\rho(x + 2d) = \rho(x)$. Eq.(7) implies a discontinuous change in the first derivative of ρ_f at $\pm d$. Similarly, between two boundaries, where the attractive interaction due to kinetochore is absent one obtains by integrating Eq.(3)

$$\left[\frac{\partial^3 \rho_f}{\partial x^3}\right]_{-d}^{d} - \eta_1 \left[\frac{\partial \rho_f}{\partial x}\right]_{-d}^{d} + \eta_2 \int_{-d}^{d} \rho_f(x)\, dx = 0 \tag{8}$$

Eq.(6), Eq.(7), and Eq.(8) altogether give us the full density profiles depending on the nature of the roots m_1 and m_2.

When m_1 and m_2 are purely imaginary, we have

$$\begin{aligned} \rho_f(x) &= 2C_1 cosh(m_1 x) + 2C_2 cosh(m_2 x), \\ C_1 &= \frac{\rho_s}{2[\frac{\kappa}{\bar{\alpha}} m_1 sinh(m_1 d) - cosh(m_1 d)] - 2\frac{P_1}{Q_1}[\frac{\kappa}{\bar{\alpha}} m_2 sinh(m_2 d) - cosh(m_2 d)]}, \\ C_2 &= -\frac{\rho_s}{2\frac{Q_1}{P_1}[\frac{\kappa}{\bar{\alpha}} m_1 sinh(m_1 d) - cosh(m_1 d)] - 2[\frac{\kappa}{\bar{\alpha}} m_2 sinh(m_2 d) - cosh(m_2 d)]} \end{aligned} \tag{9}$$

with $P_1 = sinh(m_1 d)\{m_1^3 - m_1\eta_1 + \frac{\eta_2}{m_1}\}$ and $Q_1 = sinh(m_2 d)\{m_2^3 - m_2\eta_1 + \frac{\eta_2}{m_2}\}$.

As m_1 and m_2 become a pair of complex conjugate roots written as $m_1 = a + ib$ and $m_2 = a - ib$, we obtain a density profile given by

$$\begin{aligned} \rho_f(x) &= 4C cosh(bx) cos(ax) + 4\bar{C} sinh(bx) sin(ax), \\ C &= \frac{\rho_s}{4\frac{P_2}{Q_2}[\beta_2 - \frac{\kappa}{\bar{\alpha}}(b\alpha_1 + a\beta_1)] - 4[\alpha_2 + \frac{\kappa}{\bar{\alpha}}(a\alpha_1 - b\beta_1)]}, \\ \bar{C} &= -\frac{\rho_s}{4[\beta_2 - \frac{\kappa}{\bar{\alpha}}(b\alpha_1 + a\beta_1)] - 4\frac{Q_2}{P_2}[\alpha_2 + \frac{\kappa}{\bar{\alpha}}(a\alpha_1 - b\beta_1)]} \end{aligned} \tag{10}$$

where $C = C_1 + C_2$, $\bar{C} = C_1 - C_2$, $\alpha_1 = cosh(bd)sin(ad)$, $\beta_1 = sinh(bd)cos(ad)$, $\alpha_2 = cosh(bd)cos(ad)$, $\beta_2 = sinh(bd)sin(ad)$, $P_2 = \alpha_1\{a(a^2 - -3b^2)\} + \beta_1\{b(b^2 - 3a^2)\} + \eta_1(a\alpha_1 - b\beta_1) + \frac{\eta_2}{a^2+b^2}(a\alpha_1 + b\beta_1)$, and $Q_2 = \alpha_1\{b(b^2 - 3a^2)\} - \beta_1\{a(a^2 - -3b^2)\} - \eta_1(b\alpha_1 + a\beta_1) + \frac{\eta_2}{a^2+b^2}(b\alpha_1 - a\beta_1)$.

For real m_1 and m_2 we have,

$$\begin{aligned}
\rho_f(x) &= 2C_1 cos(m_1 x) + 2C_2 cos(m_2 x), \\
C_1 &= \frac{\rho_s}{2[\frac{\kappa}{\bar{\alpha}} m_1 sin(m_1 d) + cosh(m_1 d)] - 2\frac{P_3}{Q_3}[\frac{\kappa}{\bar{\alpha}} m_2 sin(m_2 d) + cos(m_2 d)]}, \\
C_2 &= -\frac{\rho_s}{2\frac{Q_3}{P_3}[\frac{\kappa}{\bar{\alpha}} m_1 sin(m_1 d) + cos(m_1 d)] - 2[\frac{\kappa}{\bar{\alpha}} m_2 sin(m_2 d) + cos(m_2 d)]}
\end{aligned} \tag{11}$$

with $P_3 = sin(m_1 d)\{m_1^3 + m_1\eta_1 + \frac{\eta_2}{m_1}\}$ and $Q_3 = sin(m_2 d)\{m_2^3 + m_2\eta_1 + \frac{\eta_2}{m_2}\}$.

ACKNOWLEDGEMENTS

We thank Ina Poser, Tony Hyman, Alexey Khodjakov, Casper Hoogenraad, and Neda Slade for cells, plasmids, and chemicals, Juraj Simunić and Martina Manenica for help with pilot experiments, Ivana Šarić for the drawings, and all members of Tolić and Pavin groups for helpful discussions. This work was funded by the European Research Council (ERC Synergy Grant, GA Number 855158, granted to I.M.T. and N.P.), the Croatian Science Foundation (HRZZ, project PZS-2019-02-7653 granted to I.M.T.), and projects co-financed by the Croatian Government and European Union through the European Regional Development Fund — the Competitiveness and Cohesion Operational Programme: IPSted (Grant KK.01.1.1.04.0057) and QuantiXLie Center of Excellence (grant KK.01.1.1.01.0004).

AUTHOR CONTRIBUTIONS

I.M.T., M.B., and N.P. conceived the project. J.M. performed and analyzed all experiments, except the experiments with lagging kinetochores and PRC1 and CENP-E overexpression, which were done by M.Ć. M.B. provided conceptual contribution. S.G. developed the theoretical model. I.M.T. and N.P. supervised the experimental and theoretical work, respectively. I.M.T., J.M., and N.P. wrote the paper with input from all authors.

COMPETING INTERESTS

The authors declare no competing interests.

1185 **SUPPLEMENTARY MATERIALS**

1186

Supplementary Figure 1

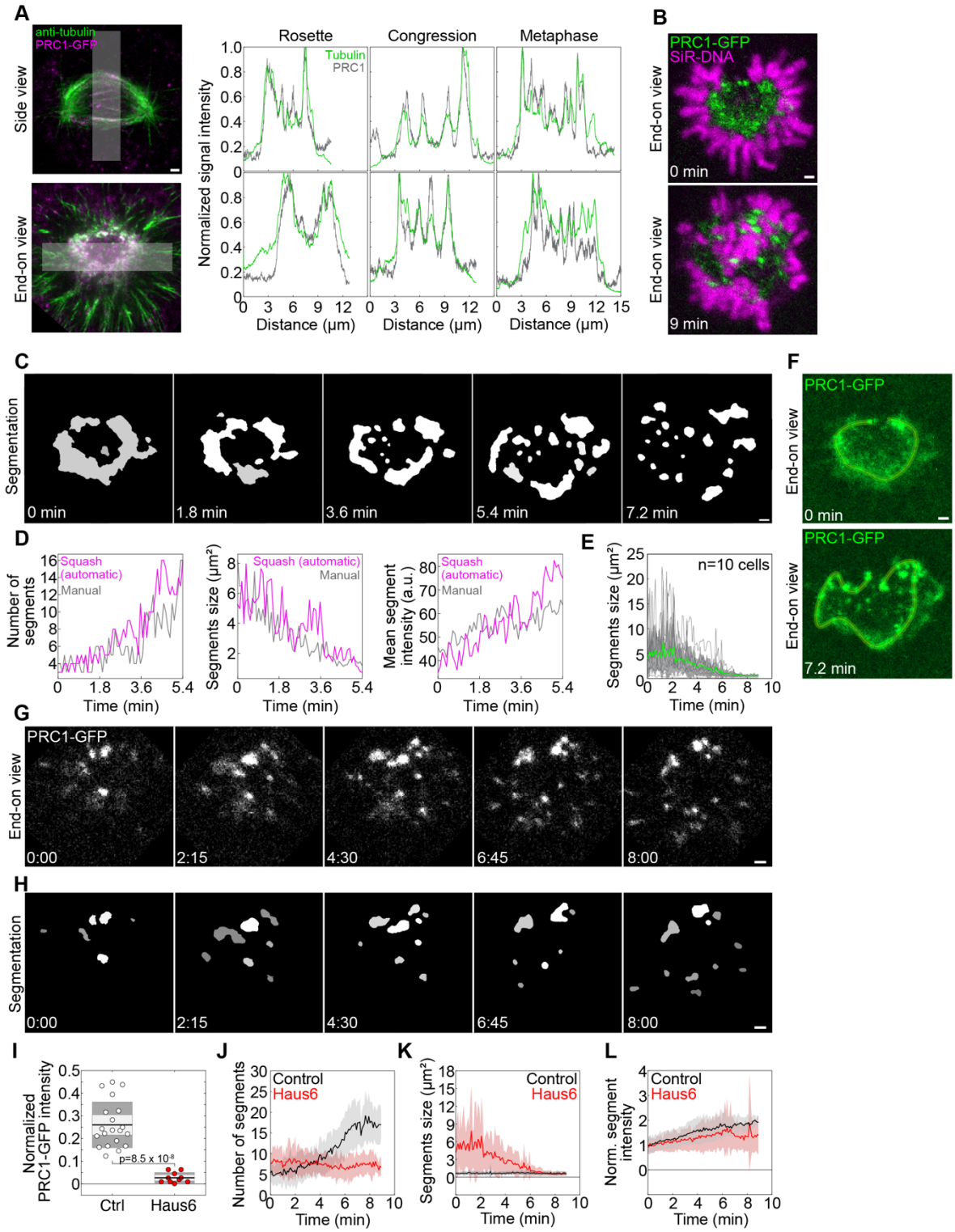

1187

1188 **Extended Data Fig. 1: Additional characterization of the network-to-bundles transition**
1189 **of PRC1-crosslinked microtubules.**
1190 **a**, STED images of tubulin (green) and confocal images of PRC1 (magenta) from Fig. 1a, with
1191 superimposed lines drawn in Fiji (left) used to measure line intensity profiles on horizontally
1192 oriented spindles (top), and vertically oriented spindles (bottom) in different phases as
1193 indicated (right). Both PRC1-GFP and anti-tubulin intensity profiles are shown. Intensity is
1194 normalized to the maximum value. Note the colocalization of the PRC1 and tubulin signal. **b**,
1195 Midplane of a vertically oriented spindle in a HeLa-Kyoto BAC cell stably expressing PRC1-
1196 GFP (green) with DNA labeled by SiR-DNA (magenta), before (top) and after (bottom)
1197 antiparallel bundle formation (9 minutes). **c**, Squash segmentation results for time-lapse images
1198 of the midplane of a vertically oriented prometaphase spindle in a HeLa-Kyoto BAC cell stably
1199 expressing PRC1-GFP corresponding to Fig. 1b. **d**, Validation of the squash segmentation
1200 method by manual measurements on a representative spindle. Graphs show the number of
1201 segments, their size and mean intensity (from left to right). **e**, Mean size of PRC1 segments in
1202 the midplane over time in HeLa-Kyoto BAC cells stably expressing PRC1-GFP, obtained using
1203 squash segmentation. Gray lines represent individual cells, green line the mean and gray areas
1204 the standard deviation (n=10 cells in 10 independent experiments). **f**, Lines drawn in Fiji along
1205 the periphery of the spindle midplane, where the PRC1 network is located in prometaphase,
1206 which were used to measure line intensity profiles in Fig. 1e,f. **g**, Time lapse images of the
1207 midplane (single plane) of a vertically oriented prometaphase spindle in a Haus6-depleted
1208 HeLa-Kyoto BAC cell stably expressing PRC1-GFP, starting with the prometaphase rosette.
1209 Time is shown in minutes:seconds. **h**, Squash segmentation results of the images shown in **g**.
1210 **i**, Mean intensity of PRC1-GFP in a region on the opposite side of the bundles that lack
1211 chromosomes in the early prometaphase network in control (n=20) and Haus6-depleted (n=10)
1212 HeLa cells expressing PRC1-GFP. PRC1-GFP intensity is normalized to the cytoplasmatic
1213 PRC1-GFP intensity. **j**, Number of PRC1 segments in the midplane over time in Haus6-
1214 depleted (red) and control (black, gray) HeLa-Kyoto BAC cells stably expressing PRC1-GFP
1215 (n=10 cells for control and 9 cells for Haus6 depletion), obtained using squash segmentation.
1216 Colored surfaces around the central lines (mean) represent standard deviation. **k**, Segment size
1217 and **l**, normalized segment intensity of PRC1-GFP segments from the same cells as in **j**. All
1218 scale bars, 1 µm.

Supplementary Figure 2

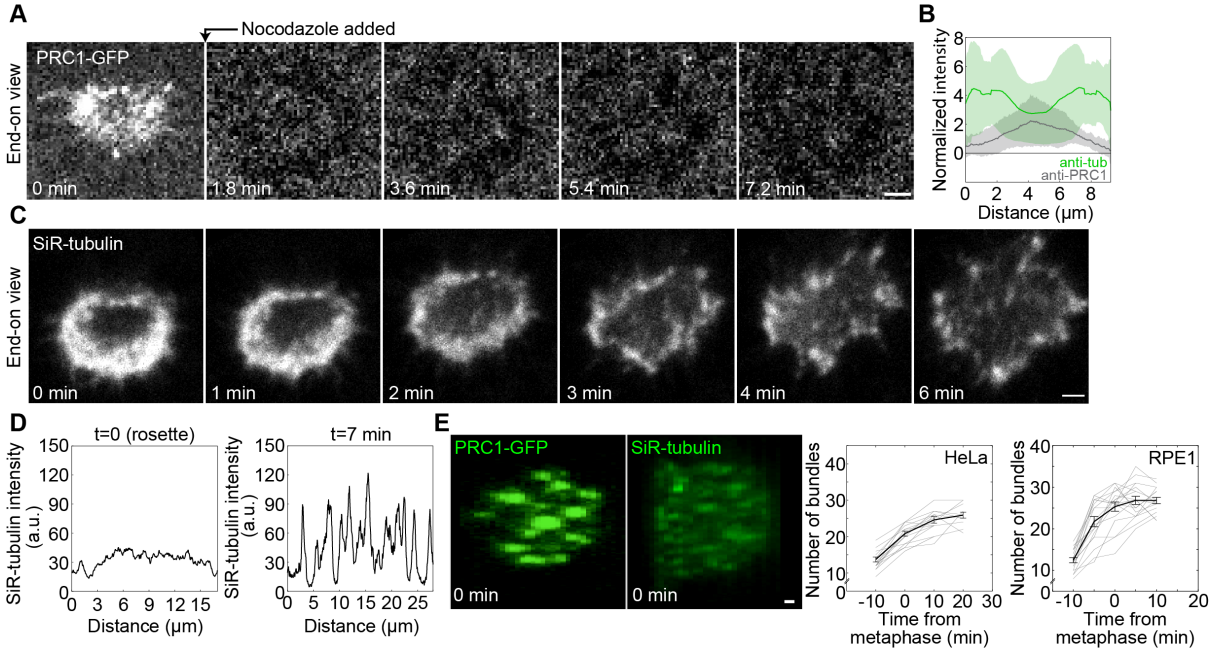

Extended Data Fig. 2: Additional characterization of PRC1 and tubulin during bundle formation.

a, Time lapse images of the midplane (single plane) of a vertically oriented prometaphase spindle in a HeLa-Kyoto BAC cell stably expressing PRC1-GFP, starting with the prometaphase rosette. Time when nocodazole was added is indicated. **b**, Intensity line plots of the anti-PRC1 (gray) and anti-tubulin (green) signal along the pole-to-pole axis in horizontally oriented early prometaphase spindles (rosette stage) of non-transfected immunostained HeLa cells, n=20 cells from 2 independent immunostainings. Intensity was normalized to the cytoplasmatic anti-PRC1 and anti-tubulin intensity, respectively. Note that the PRC1 intensity is highest in the middle of the spindle, whereas tubulin intensity is highest away from the middle, i.e., close to the poles. **c**, Time lapse images of the midplane (single plane) of a vertically oriented prometaphase spindle in a HeLa-Kyoto BAC cell stably expressing PRC1-GFP and stained with SiR-tubulin, starting with the prometaphase rosette. Only SiR-tubulin channel was imaged. **d**, SiR-tubulin intensity line plots along the periphery of the spindle midplane at t=0 and t=7 minutes from the cell shown in **c**. **e**, Reconstructed (rotated by 90 degrees) images of the midplane of a horizontally oriented spindle in a HeLa-Kyoto BAC cell stably expressing PRC1-GFP (left image) and in an hTERT-RPE1 cell expressing CENP-A-GFP and centrin1-GFP labeled with SiR tubulin (right image). Graphs show the number of bundles over time for the HeLa cell line (left, n=12 cells) and the RPE1 cell line (right, n=16

1240 cells), corresponding to the images on the left. Time zero is the beginning of metaphase. All
1241 scale bars, 1 μm.

Supplementary Figure 3

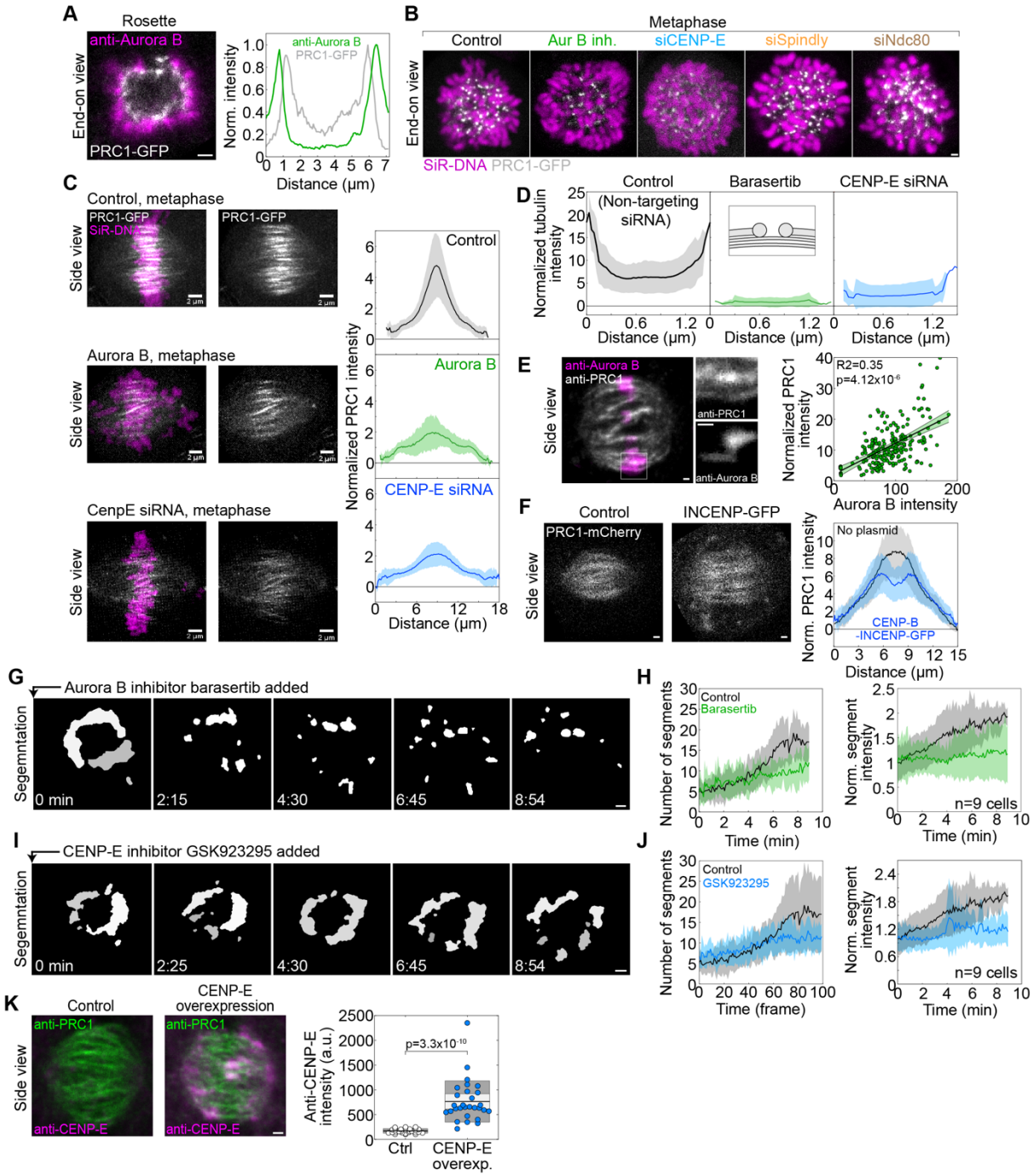

Extended Data Fig. 3: Additional characterization of the role of kinetochores in overlap bundle formation.

a, Left, image of a vertically oriented prometaphase rosette immunostained for Aurora B (magenta) in a HeLa-Kyoto BAC cell stably expressing PRC1-GFP (white). Right, intensity line plot of PRC1-GFP (grey) and anti-Aurora B (green) along a line drawn across the spindle cross-section, passing through the center. Line thickness was 1/3 of the spindle cross-section.

1250 Intensity is normalized to the maximum value for each channel. **b**, Images of vertically oriented
1251 metaphase spindles in a HeLa-Kyoto BAC cell line stably expressing PRC1-GFP (white) from
1252 Fig. 2e. Chromosomes are labeled with SiR-DNA (magenta) to show the metaphase plate. **c**,
1253 Live-cell images of horizontally oriented metaphase spindles in HeLa-Kyoto BAC cells stably
1254 expressing PRC1-GFP (white) and stained with SiR-DNA (magenta). Control (top), Aurora B
1255 inhibition (middle) and CENP-E depletion (bottom). Maximal projections of 41 planes are
1256 shown. The corresponding intensity line profiles of PRC1-GFP are shown to the right, mean
1257 (central line) and standard deviation (colored surface). The line profiles were measured along
1258 a line drawn from pole to pole. Line thickness was 1/3 of the spindle width. Intensity was
1259 normalized to the cytoplasmatic PRC1 intensity. Scale bars, 2 µm. Number of cells: 56 for
1260 control, 32 for Aurora B inhibition, 43 for CENP-E siRNA. All measurements are from 3
1261 independent experiments. **d**, Intensity line profiles corresponding to anti-tubulin signal in the
1262 bridging fiber from Fig. 2f,g and Fig. 3b,c; mean (central line) and standard deviation (colored
1263 surface); n=22 bundles from 14 cells for control, 11 bundles from 9 cells for Aurora B
1264 inhibition, and n=10 bundles from 7 cells for CENP-E siRNA, from 3 independent
1265 immunostainings. Intensity was normalized to the cytoplasmatic anti-tubulin intensity. **e**,
1266 Image of a spindle immunostained for Aurora B (magenta) and PRC1 (white) in an
1267 untransfected HeLa cell in metaphase. Sum of 5 planes is shown. Enlargements of anti-PRC1
1268 and anti-Aurora B (both in white) within the square marked on the main image are shown to
1269 the right. Graph shows correlation between anti-PRC1 and anti-Aurora B signal on the
1270 corresponding centromere, n=404 PRC1-Aurora B pairs from 26 cells. Intensity was
1271 normalized to the cytoplasmatic anti-PRC1 and anti-Aurora B intensity, respectively. **f**, Live
1272 cell images of metaphase spindles in HeLa cells transfected with PRC1-mCherry (white) in a
1273 control cell (left image) and a cell transfected with CENP-B-INCENP-GFP construct (right
1274 image). Maximal projections of 41 planes are shown. Graph shows intensity line plots of
1275 PRC1-mCherry along the spindle main axis, mean (central line) and standard deviation
1276 (colored surfaces), n=29 cells for control and n=28 for CENP-B-INCENP-GFP, 3 independent
1277 experiments per condition. Intensity was normalized to the cytoplasmatic PRC1 intensity. **g**,
1278 Squash segmentation results for time-lapse images of the midplane of a Barasertib-treated
1279 vertically oriented prometaphase spindle in a HeLa-Kyoto BAC cell stably expressing PRC1-
1280 GFP, corresponding to Fig. 2j. **h**, Number of PRC1 segments (left) and normalized mean
1281 intensity of PRC1 segments (normalized to the intensity at t=0, right) over time from squash
1282 segmentation in control and Barasertib-treated (i.e., Aurora B-inhibited) cells, as indicated.
1283 Colored surfaces around the central lines (mean) represent standard deviation, n=9 cells from

9 independent experiments. **i**, Squash segmentation results and **j**, the related quantification for cells treated with the CENP-E inhibitor GSK923295, corresponding to Fig. 3f. Legend as in **g** and **h**, respectively, n=9 cells from 9 independent experiments. **k**, Images of horizontally oriented spindles in metaphase, immunostained for PRC1 (green) and CENP-E (magenta), in a control HeLa cell (left image) and after CENP-E overexpression (right image). Graph shows total CENP-E intensity on the spindle in control cells and after CENP-E overexpression, n=29 cells in each condition from 3 independent experiments. The black line shows the mean; the light and dark grey areas mark 95% confidence interval on the mean and standard deviation, respectively. Note that the overexpression level is roughly 5-fold. In all controls for siRNA experiments the cells were transfected with nontargeting siRNA. All scale bars except in **c**, 1 µm.

Supplementary Figure 4

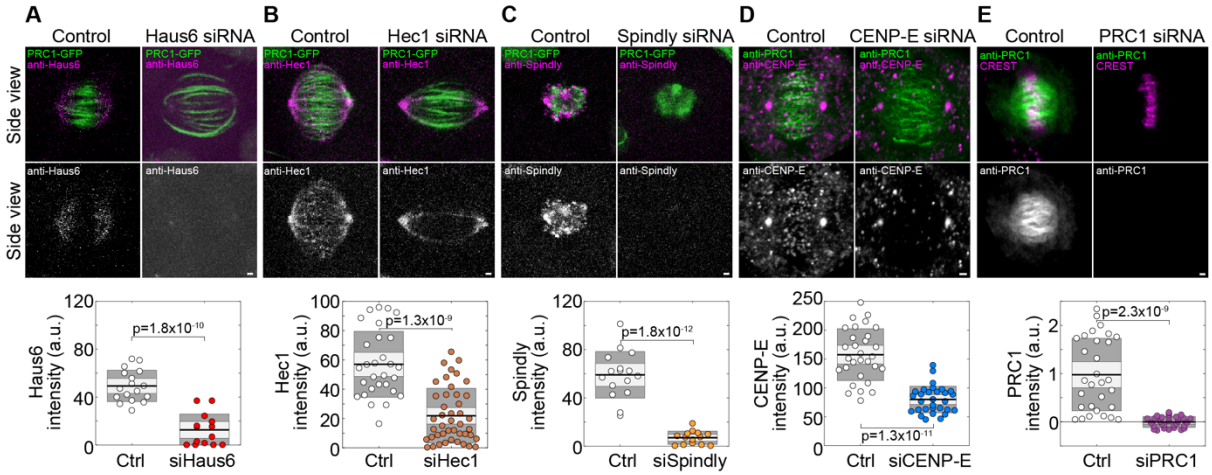

Extended Data Fig. 4: Quantification of protein depletion by immunostaining.

In each panel the images show control and depleted spindles, as indicated, with merged channels in the first row and only the channel of the depleted protein (white) in the second row. The graph under the images shows the quantification of the total signal intensity of the indicated protein on the spindle in control and depleted cells. For Hec1 depletion and the corresponding control, the total intensity of anti-Hec1 signal was measured in a region encompassing all DNA, i.e., excluding the poles. In **a-c**, HeLa-Kyoto BAC cell line stably expressing PRC1-GFP was used, whereas in **d**,**e**, untransfected HeLa cells were used. The number of cells was: (**a**) control, n=17, and Haus6 depletion, n=14, (**b**) control, n=29, and Hec1 depletion, n=44, (**c**) control, n=16, and Spindly depletion, n=14, (**d**) and (**e**), n=30 for each condition. Mean silencing was: (**a**) 74%, (**b**) 62%, (**c**) 90%, (**d**) 51%, (**e**) ~100% when the background signal is subtracted (data shown in panel **e**) and 86% without background subtraction (data not shown). In all control experiments the cells were transfected with nontargeting siRNA. All scale bars, 1 µm.

Supplementary Figure 5

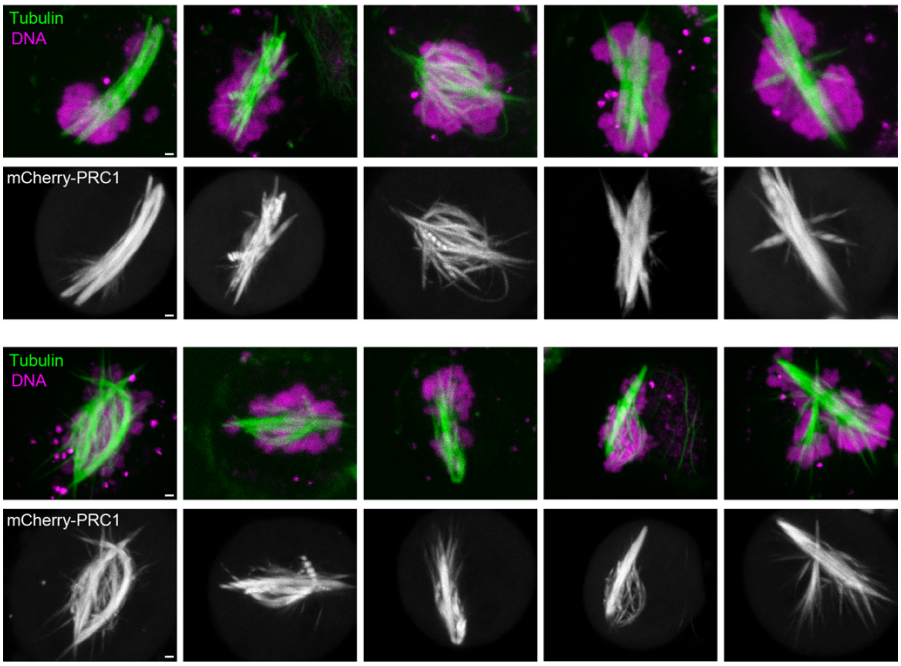

Extended Data Fig. 5: Additional images of spindles in cells with overexpressed PRC1. Examples of 10 spindles with overexpressed PRC1 in HeLa-TDS cells. Merged images show microtubules (SiR-tubulin, green) and DNA (Hoechst 33342, magenta), and the corresponding single-channel images below the merged ones show PRC1-mCherry (white). Scale bars, 1 µm.

1317 **SUPPLEMENTARY VIDEOS**

1318

1319 **Supplementary Video 1. Overlap bundle formation during early prometaphase.**
1320 Time lapse of a midplane of a vertically oriented prometaphase spindle in a HeLa-Kyoto BAC
1321 cell stably expressing PRC1-GFP starting with prometaphase rosette. A single plane is shown.
1322 Time interval between acquired images is 5.4 seconds. Time is shown in minutes:seconds.
1323 Scale bar, 1 µm.

1324

1325 **Supplementary Video 2. Bundle formation after Haus6 (augmin subunit) depletion.**
1326 Time lapse of a midplane of a vertically oriented prometaphase spindle in a Haus6-depleted
1327 HeLa-Kyoto BAC cell stably expressing PRC1-GFP starting with prometaphase rosette. A
1328 single plane is shown. Time interval between acquired images is 5.4 seconds. Time is shown
1329 in minutes:seconds. Scale bar, 1 µm.

1330

1331 **Supplementary Video 3. Bundle formation after Aurora B inhibition.**
1332 Time lapse of a midplane of a vertically oriented prometaphase spindle in a HeLa-Kyoto BAC
1333 cell stably expressing PRC1-GFP starting with prometaphase rosette. Barasertib was added just
1334 before the beginning of the movie. A single plane is shown. Time interval between acquired
1335 images is 5.4 seconds. Time is shown in minutes:seconds. Scale bar, 1 µm.

1336

1337 **Supplementary Video 4. Bundle formation after CENP-E inhibition.**
1338 Time lapse of a midplane of a vertically oriented prometaphase spindle in a HeLa-Kyoto BAC
1339 cell stably expressing PRC1-GFP starting with prometaphase rosette. GSK923295 was added
1340 just before the beginning of the movie. A single plane is shown. Time interval between acquired
1341 images is 5.4 seconds. Time is shown in minutes:seconds. Scale bar, 1 µm.

1342

1343 **Supplementary Video 5. Movement of overlap bundles during prometaphase.**
1344 Left, time lapse of a midplane of a vertically oriented prometaphase spindle in a HeLa-Kyoto
1345 BAC cell stably expressing PRC1-GFP starting with prometaphase rosette. The images were
1346 translated so that the position of the two bright bundles that are initially found in the upper
1347 region of the spindle is roughly constant. A single plane is shown. Time interval between
1348 acquired images is 2.7 seconds. Right, trajectories of the bundles from the movie on the left.
1349 Time is shown in minutes:seconds. Scale bar, 1 µm.

1350

1351 **Supplementary Video 6. Chromosome congression to the spindle midplane causes spindle**
1352 **widening, end-on view.**
1353 Time lapse of the central part of a vertically oriented prometaphase spindle in a HeLa-Kyoto
1354 BAC cell stably expressing PRC1-GFP (green) starting with prometaphase rosette. DNA is
1355 stained with SiR-DNA (magenta). Maximum projection of 3 middle planes is shown. Time
1356 interval between acquired images is 30 seconds. Time is shown in minutes:seconds. Scale bar,
1357 1 μm.
1358
1359 **Supplementary Video 7. Chromosome congression to the spindle midplane causes spindle**
1360 **widening, side view.**
1361 Time lapse of a horizontally oriented prometaphase spindle in a HeLa-Kyoto BAC cell stably
1362 expressing PRC1-GFP (green) starting with prometaphase rosette. DNA is stained with SiR-
1363 DNA (magenta). Sum of 41 planes is shown. Time interval between acquired images is 30
1364 seconds. Time is shown in minutes:seconds. Scale bar, 1 μm.